Journal of Geomorphology, Vol. 1/1 (2022), 1–24
Published Early Access September 22, 2020, published online December 2022

Open-Access Article

Calanchi badlands reconstructions and long-term change detection analysis from historical aerial and UAS image processing

Manuel Stark[1,*], Fabian Neugirg[2], Andreas Kaiser[3], Marta Della Seta[4], Jürgen Schmidt[5], Michael Becht[1] and Florian Haas[1]

[1] Chair of Physical Geography, Catholic University of Eichstätt-Ingolstadt, Eichstätt, 85072, Germany
[2] Municipal administration, Strömsund, 83324, Sweden
[3] Department of Geography, Friedrich Schiller University, Jena, 07743, Germany
[4] Department of Earth Sciences, Sapienza University of Rome, Rome, 00185, Italy
[5] Soil and Water Conservation Unit, TU Bergakademie Freiberg, Freiberg, 09599, Germany
* Corresponding author: mstark@ku.de

With 15 figures and 10 tables

Abstract: In Italy, highly dissected badlands may be found widespread (over the entire Apennine region) and are locally described as "calanchi" (singular: "calanco"). Accelerated geomorphic processes led to the rapid evolution of these erosional landunits with intense drawbacks on agriculture, infrastructure and society. Historical aerial photographs (HAP) of such badland areas exist worldwide. To reconstruct the past surface and related topographic changes offers high potential for the assessment of long-term topographic changes of many interesting landscapes. Due to technical and conceptual demands of traditional photogrammetry those photographs have been used comparable little in long-term geomorphology. Processing them with user-friendly SfM-MVS photogrammetry would provide a new perspective on the assessment of long-term erosion rates on the catchment and slope scale and the related badland evolution. Therefore, this multi-temporal approach focusses on the appliance of SfM-MVS photogrammetry in order to reconstruct the past landscape and to calculate the related long-term surface changes of a badland located in the upper Val d'Orcia (Tuscany, Italy). The analysis is based on a set of high-resolution UAV images (2016) and two sets of historical aerial images of varying quality and scale (1976 and 1994). Digital elevation models (DEMs), shaded relief raster, several morphometric parameters and DEMs of difference (DoD) (resolution: 1 m) were used to obtain overall terrain changes and to calculate sediment balances and annual surface change rates on catchment and slope scale. Change detection analysis revealed a mean surface lowering of 0.01 $m*a^{-1}$ (1976–2016) on the catchment scale and 0.03 $m*a^{-1}$ (1976–1994) to 0.06 $m*a^{-1}$ (1994–2016) on the slope scale. Our results further show a reduced activity of fluvial erosion processes from the mid 90s' on while mass movements dominating the topographic changes in the second half of the 40 years observation period. Erosion processes are enhanced near the tear-off edges of the lateral valleys. Deposition mainly occurs in the main valley floor which can be classified as a temporary sediment sink/store. The geomorphic development of the catchment indicates a self-stabilizing behaviour towards an equilibrium state. A reduction of the mean slope gradient in the main valley from 25° in 1976 to 14° in 2016 confirms the self-stabilizing theory. The study also revealed the potential and limitations of historical aerial images for long-term geomorphic change detection and showed that SfM-MVS algorithms operate less reliable when applied to only a few images (n=3) of a singular flightline. Nevertheless, the good agreement of our results with the long term rates obtained by other authors with different methods/techniques and different time scales proof the great potential of historical aerial photographs for 3D surface reconstructions (SfM-MVS) of semi-arid badlands when ceratin quality parameters, mainly high image overlaps and entropy, are fulfilled.

Keywords: High-resolution topography; historical aerial photographs; unmanned aerial systems (UAS); Structure from Motion (SfM); Multi-View-Stereo (MVS); quantitative analysis; sediment balancing; badland development

DOI: 10.1127/jgeomorphology/2020/0658
© 2020 The authors
Gebrüder Borntraeger Science Publishers, Stuttgart, www.borntraeger-cramer.de

1 Introduction and state of research

In the Mediterranean region distinctive geologic and climate settings lead to enhanced slope-degradation processes and favour the development of many badlands (Clarke & Rendell 2000, Faulkner 2013). Especially regions of semi-arid climates, with concentrated rainfall in autumn and winter and dry summer months, face intense drawbacks on agriculture, infrastructure and society due to accelerated denudation and erosion processes (Castaldi & Chiocchini 2012). Although fluvial processes are dominant, landslides, both translational and rotational, as well as soil creep and debris flows are of crucial importance for the development of steep slopes in unconsolidated material (Becht 1986), typical for badlands in marine lithologies. These erosional landscapes can be described as runoff source areas (Cantón et al. 2018) characterized by highly erodible substrate and bare or sparsely vegetated terrain (Moreno-de las Heras & Gallart 2018). Their geomorphological evolution and land degradation have been studied worldwide (e.g. Adugna et al. 2015, Cánovas et al. 2017, Kaiser et al. 2014, Llena et al. 2020, Zhang et al. 2016). In Europe, most studies were carried out around the Mediterranean (e.g. Bucciante 1922, Cerda et al. 2016, Ciccacci et al. 2008, Della Seta et al. 2007, Llena et al. 2020, Nadal-Romero et al. 2010). In Italy, specific climatic and lithological conditions lead to the development of widespread badlands in the Plio-Pleistocene marine clays of the Calabrian deposits and the *blue clays* of the Apennine piedmont (Bollati et al. 2012), locally described as calanco (singular)/ calanchi (plural).

A variety of definitions of the term "calanco/calanchi" are given in the literature. Castiglioni (1979) defines calanchi as a group of minor valleys with steep slopes, sparse vegetation, a rapid morphological evolution. According to Rodolfi & Frascati (1979) and Moretti & Rodolfi (2000), those denudation "hot spots" (Della Seta et al. 2009) can be separated in the three different morphological types "A", "B" and "C": "Type A" is defined by a system of narrow but deep cuts, separated by thin edges and ridges with concentrated surface runoff which leads to sharp and dissected landforms in the clayey substrata. The drainage pattern is dense and channel profiles show a typical V-shape. Type B evolves typically from recurring superficial slides and mudflows on un-weathered substrata and forms a trough-valley-system, separated by small convex ridges. Type C is affected by a higher frequency of mass movements and frequently occurring landslides are about to destroy the ridges while filling up the bottom of the valley floor with deposits (Ciccacci et al. 2008). Note that valley floors get filled in all calanchi types and that the distinction of type A and B may not always be unambiguous at first sight. Depending on whether if fluvial- or mass-wasting processes are the dominant process in the catchment it will be classified as type A (v-shaped valleys), type B (trough-valleys) or type C. Gallart et al. (2013) underline the complexity of the system by describing badlands as full-size laboratories that offer a unique learning source where many processes can be observed or experimented by a wide variety of techniques and field measurements. In the *Val d'Orcia badlands* in Southern Tuscany, field monitoring campaigns and calculation of erosion rates have been performed (c.f. Table 1), inter alia, by Della Seta et al. (2007), Ciccacci et al. (2003), (2008) and (2009), Aucelli et al. (2016) and Neugirg et al. (2016). The studies have different focuses in terms of methodology but also in terms of temporal and spatial resolution. Most of these studies have been carried out on test plots using erosion pins or LiDAR measurements which allow for accurate point measurements and in the case of LiDAR for a very high spatial resolution within the single test plots. Depending on the investigation design (number of plots, length of the investigation period, repetition rate), the studies were able to draw conclusions about the mean annual erosion and accumulation rates on badlands. Due to the focus on test plots, most of the existing works are limited in both space and time and thus have to extrapolate (regionalize) their results for wider areas. But this extrapolation typically leads to the problem that geomorphic processes with low frequencies and high magnitudes

Table 1. Surface change rates in the Val d'Orcia badlands obtained by selected authors including the applied methods and observation period.

Authors	Method	Annual surface lowering	Observation period
Ciccacci et al. 2003	Erosion pins	2–3 cm a^{-1}	5 1/2 years
Ciccacci et al. 2009	Erosion pins	6–6.5 cm a^{-1}	5 1/2 years
Aucelli et al. 2012	Photogrammetric analysis on historical aerial photographs	1.1–5.5 cm a^{-1}	27 years
Aucelli et al. 2016	Photogrammetric analysis on historical aerial photographs	6.2 cm a^{-1}	27 years
Neugirg et al. 2016	UAV-SfM and TLS	5.3 cm a^{-1}	One year

are (i) underestimated or even not included in the results or (ii) if they appear within the investigation areas are possibly overestimated.

To increase the size of the investigation area in order to include also high-magnitude events, we want to make use of the structure-from-motion (SfM) and multiple-view-stereo (MVS) algorithms which have been shown to greatly improve the study of geomorphic processes in hardly accessible areas (Brandolini et al. 2018). Numerous studies (e.g. Haas et al. 2015, Neugirg et al. 2016, Smith & Vericat 2015), already proved the ability of SfM-MVS to reconstruct topographic surfaces of a complex landscape on basis of high-resolution image networks obtained by low altitude airborne (Zhang et al. 2018) or terrestrial photography (Piermattei et al. 2016).

Mölg & Bolch (2017) showed that SfM-MVS algorithms are able to produce DTMs of at least similar quality in a third to a sixth of time effort when compared to conventional photogrammetric methods. A successful appliance of combined SfM-MVS methods to historical aerial photographs (HAP) of calanchi areas would offer a new perspective on the assessment of long-term erosion rates on the catchment and slope scale and the related badland evolution. Thus we want to test the ability of SfM-MVS for surface reconstruction and erosion rate assessment on the basis of HAP and present-day UAS photographs. By doing so, we will be able (i) to include geomorphic processes with low frequencies and high-magnitude into the analysis of the morphological spatio-temporal evolution of a calanchi landscape over a time span of 40 years (1976–2016) and (ii) to calculate the related annual surface change rates which can be used for the validation of those rates that were obtained over shorter periods (by e.g. Neugirg et al. 2016 or Della Seta et al. 2009) or by different photogrammetric methods (Aucelli et al. 2016). The present analysis is carried

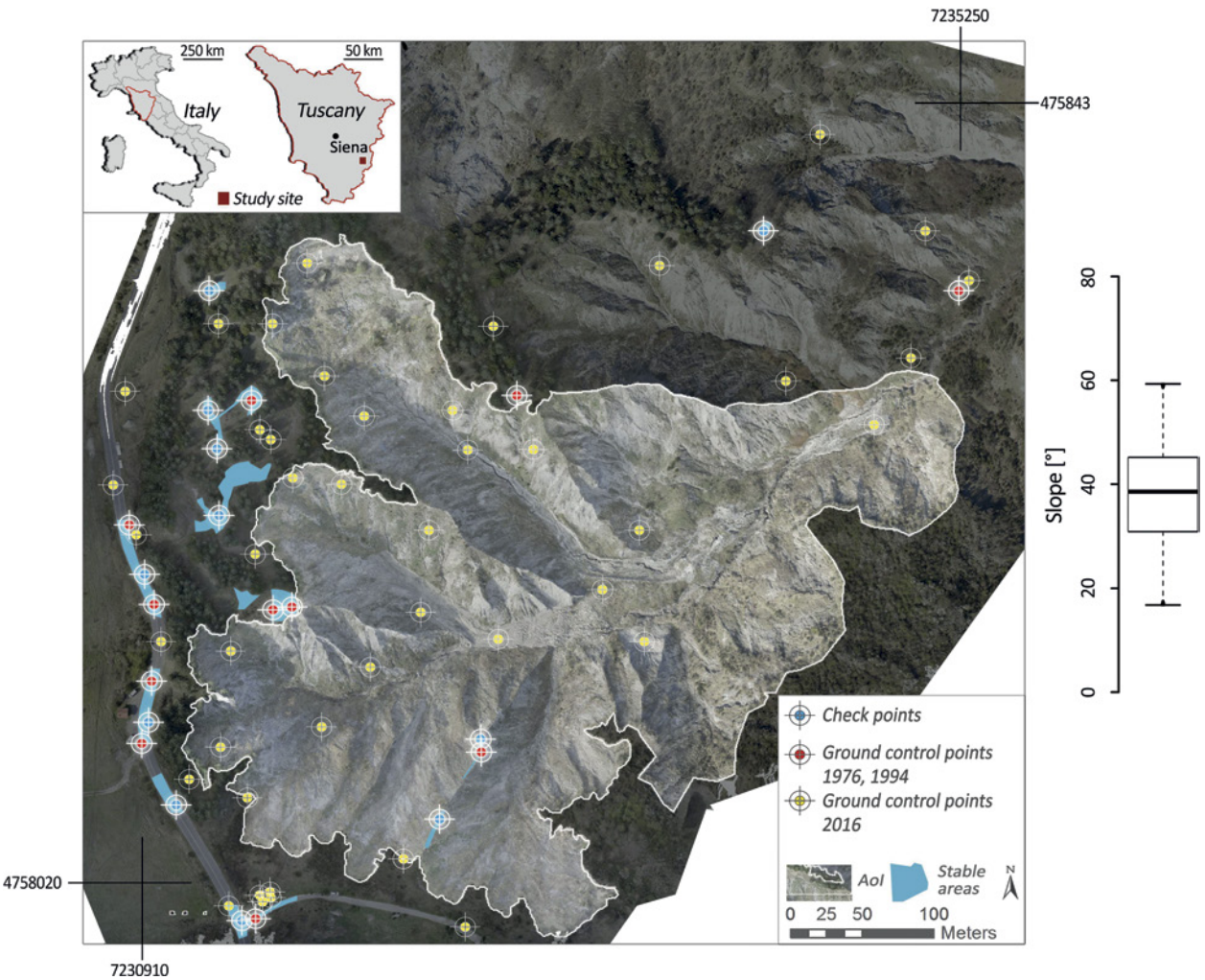

Fig. 1. Study area with AoI and locations of GCPs (yellow dots: 2016; red dots: 1976 & 1994), CPs (blue dots) and stable areas (blue polygons) (top); boxplot of slope inclination (right).

out on two sets of HAP (1976 and 1994) and one network of high-resolution images (2016) that were taken by an UAS in an on-site campaign in April 2016.

2 Study area

The study site is located on the Tyrrhenian side of Central Italy within the Tuscan Pre-Apennines about 6 km NNW of the town Radicofani (Province Siena, Fig. 1). The area of interest (AoI) spans an altitude from 501–651 m a.s.l. and an area of about 109,000 m^2. It forms part of the Upper Orcia River basin (*Val d´ Orcia*) and the drainage pattern of the AoI is structurally controlled by the Radicofani Graben (NW–SE) and the Scalonca stream (SW–NE / main valley of the AoI) which enters the River Orcia about 1 km downstream of the calanchi heads. Slopes are barely vegetated with most frequent inclination classes between 25° and 50°. Mean thalweg gradient is 14° in the main valley and 27° in the tributary valleys. The AoI is dominated by aspects from the north-east to the south-east with a maximum in the class SSE and a minimum in SWW. Nowadays, grazing ground and agricultural land cover most of the Radicofani area, while woods (mainly degraded macchia) are restricted to small fragmented portions. Reforestation practices with frugal conifers, such as the Italian cypress, the Arizona cypress and the black pine have been carried from more than 50 years but an invasion of natural vegetation in the reforested areas has not been recognized (Castaldi & Chiocchini 2012).

The tectonic history is representative of the general orogenic history of the Northern Apennines, where Cretaceous to early Oligocene deposits occurred in compressive forelands (Ciccacci et al. 2008). A regional arching of the Apennine in the Quaternary raised the slightly NE tilting clayey lithological unites several hundreds of meters (Acocella & Rossetti 2002). Today, these erosion-prone marines and terrestrial deposits crop out in altitudes up to 900 m above mean sea level (Ciccacci et al. 2008, Vergari et al. 2011). The stratigraphic sequence of the study site is formed by numerous layers of varying thickness from 4 to 25 cm (Colica 2000). The textures vary from clay to sandy-loam with gravel present in certain conglomerate banks. Soil horizons are very sparse and have developed on a very few gentle slopes but are mainly restricted to forested surfaces which are located on the most upper area of the badland (mostly above the calanchi border).

Large parts of the surrounding area have been modified by anthropogenic activity. The widening of tilling and grazing ground as well as attempts to control the effects of intense denudation processes are just some of the well documented examples (Aucelli et al. 2016, Castaldi & Chioncchini 2012, Ciccacci et al. 2008, Vergari et al. 2011). Erosion control practices, e.g. checks and dams, were introduced in 1989 and since then, many attempts have been made to control erosion processes in those areas where runoff is extremely high and mass movements particularly intense. In 1992, most of the constructions were already seriously damaged and in 1996 all installations have been destroyed by erosional processes (Colica 2000). Damaged infrastructure (power poles, streets, bridges) in the wider area testify to active erosion processes.

Climate shows a typically Mediterranean pattern with monthly mean temperatures between 3.8 °C (January) and 21.5 °C (August) and an annual mean of 12 °C (Castaldi & Chiocchini 2012). Figure 3 shows the annual precipitation from 1951 to 2016. It is quite noticeable, that the mean for the period 1961–1990 is 197.5 mm below the annual mean for the years 2003–2016. The annual mean precipitation for the observation period 1976 to 2016 is at 831.2 mm. Monthly mean precipitation is ranging between 37.6 mm in July (max: 145.4 mm) and 111 mm in November (max: 290 mm) with a secondary peak in February and March. Heavy rainfall events frequently occur in autumn and winter while summer months are rather dry.

3 Material and methods

3.1 Image networks and ground control survey

This study is carried out on two sets of grey-scaled HAP (1976 and 1994) and a set of coloured high–resolution aerial images, obtained with an UAS (2016). The 1976 data origins from the *EIRA*–flight, 1994–images were taken during the *TUSCANY REGION*–flight (Italian Military Geographical Institute (IGM) and Tuscany Region). All aerial photographs were taken following linear flight-paths. HAP were provided in tagged image file format (TIFF) with a resolution of 1200 dpi. The image sets are characterized by a low picture count, varying scale and ground sample distances as well as by varying exposure and resolution (Table 2).

Table 2. Main characteristics of HAP.

Year	1976	1994
Image count:	6	3
Approximate photo scale:	1:17,000	1:36,000
Flying altitude [m]:	2,682	5,547
Focal length nominal [mm]:	153.07	152.82
Ground pixel dimension [cm]:	37	77

Fig. 2. UAV Falcon 8 (left) and red carpet with centrally located reflector (GCP) in the study area (UAV image available at: http://www.asctec.de/ascending-technologies/uav-presse-mitteilungen/#pane-0-1 (last opened: 2019/03/24, 11:00)).

UAS survey was conducted in April 2016 with a Falcon 8 octocopter (Ascending Technologies/Intel) equipped with a calibrated Sony Nex 5 camera and a fixed Sony LES lens (APS-C sensor 15.6 × 23.5 mm, focal length: 16mm, F2.8E, 14MP resolution). The UAS is equipped with GPS, altimeter, gravity and inclination sensors. Average flying altitude was 100 m above ground. A pre-defined flight plan (AscTec Autopilot Control v1.68) was used to guarantee a sufficient overlap of 80% minimum (front- and sidelap). Flight times lasted from four to eight minutes with a total of 13 flights and a total image count of 262. 44 red carpets (0.4 m × 0.4 m) with a centrally located reflector (diameter: 0,1 m) were distributed as ground control points (GCPs) across the study area, serving for an exterior orientation (Fig. 2). The reflectors were measured using a differential GNSS rover-base system (Leica GS09). One fix point was measured with a Stonex S9III GNSS antenna making use of real-time kinematic information provided by the Italian positioning service Topcon (www.geotop.it). The fixpoint served as the base position for the Leica GS09 reference station and was used to convert all GCPs from a local to a global coordinate system (UTM 32N; EPSG: 25832).

3.2 Data processing

3.2.1 Image processing

We used a standard SfM-MVS software (PhotoScan Pro 1.4 by Agisoft) to process the HAP and UAS image networks. Figure 3 shows the entire workflow of data-processing and -analysis. A detailed explanation of the SfM-MVS workflow is given in e.g. Eltner et al. (2016).

Although Photoscan Pro allows a prior specification of the interior orientation, we chose to specify only the initial focal length and allowed the use of self-calibrated camera parameters (f, c_x, c_y, k_1, k_2, k_3, p_1 & p_2). All images were aligned and orientated with the highest alignment quality parameter and GCP-markers were set in all images to specify the exterior orientation (EPSG 25832) for the data. After the initial SfM process, a 3D point-cloud (PC) densification (MVS) was performed and orthomosaics were generated for each set of data. The PCs were exported as ASCII-.txt-files while the geo-rectified orthomosaics were stored in TIFF image format for digital mapping and visual interpretation/validation of the results.

While the processing of UAS data follows the standard principles of the SfM-MVS workflow, the HAP had to undergo certain image adjustments prior to the SfM-MVS process. As the 1976 images differ strongly in contrast and exposure from the ones of 1994, both data sets were edited using software Photoshop Pro (Adobe Creative Suite 5). After we adjusted the histogram values (greyscale) of the 1976 data (Fig. 4), the edited images were exported in TIFF file format (1200 dpi) for further processing. To exclude non-relevant areas, all images were masked according to the extent of the defined study area.

Pre-processing of HAP mainly consists of two steps:

1) All HAP were masked to exclude the black frame which includes flight information and fiducial markers.
2) The images were cropped to a common x-, y-extent (uniform number of pixels along the x- and y-axis).

Step two was necessary to ensure that Photoscan Pro recognizes that all images coming from the same source (camera). Thus, the software applies the same camera-parameters (lens-distortion parameters) to all images. After the successful alignment of each data set, 11 markers

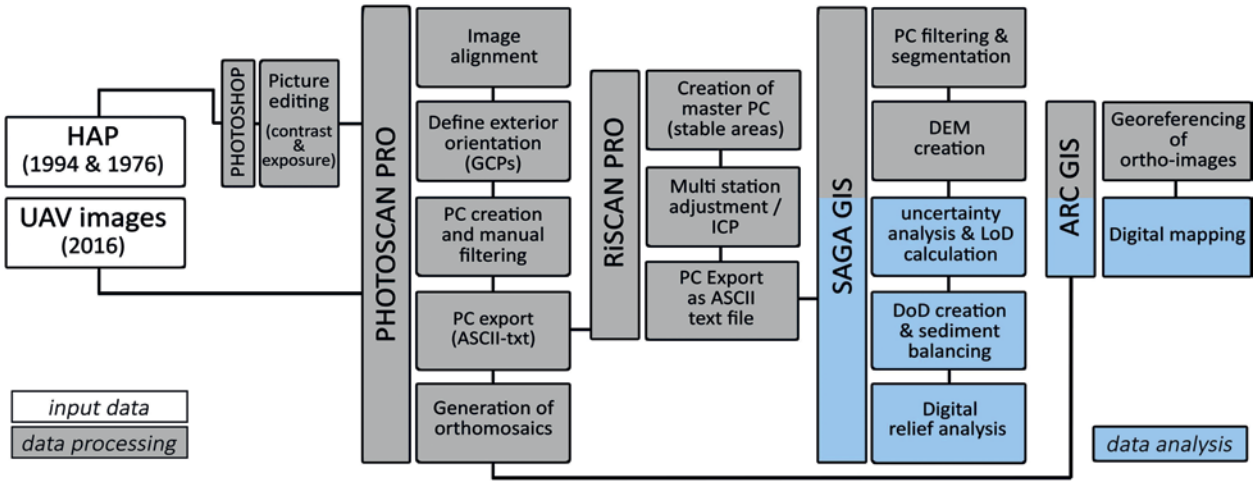

Fig. 3. Entire workflow of data-processing and -analysis.

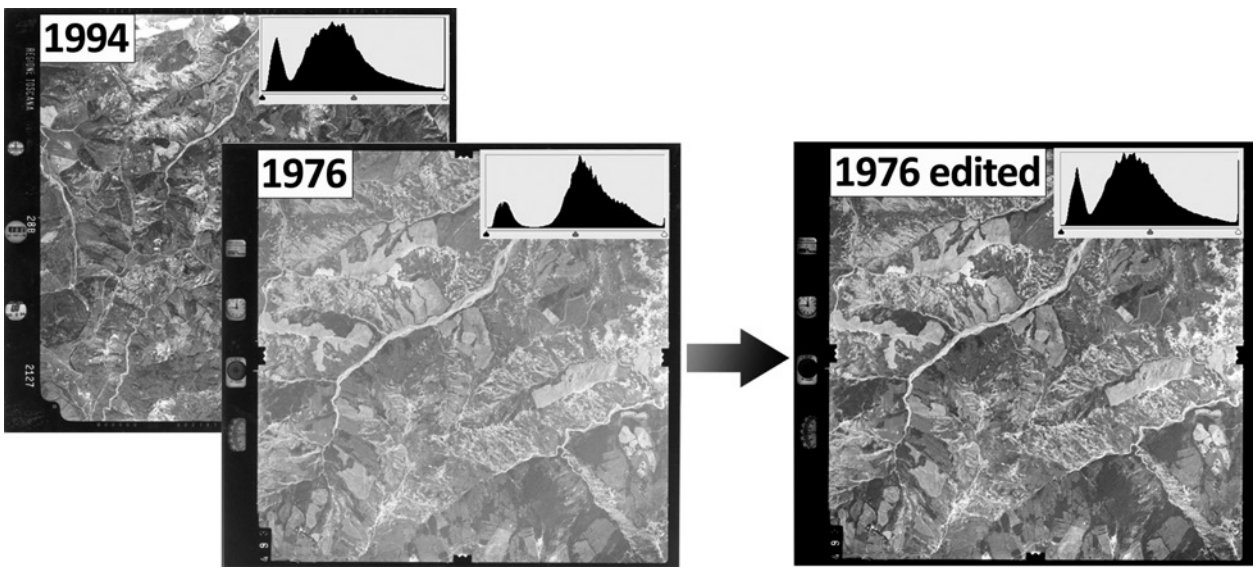

Fig. 4. 1994 and 1976 image with original histogram (left); edited 1976 image with histogram (right).

were set on both HAP sets in order to specify the locations (x-, y-, z-coordinates) of the GCPs within the scene. As HAP were provided without information on the exterior orientation global coordinates had to be extracted from the 2016 PC. As mentioned by Eltner & Schneider (2015), the GCP residuals depend on the weighting of observations in the adjustment and might not be representative of the actual global accuracy of the surface points. As we assume surface changes within most parts of the AoI in 40 years (1976–2016) the GCPs used for the co-registration were set on well identifiable objects in stable areas (Bennett et al. 2012, Haas et al. 2015, Westaway et al. 2000) that had not undergone visible surface changes in the monitoring epoch. In fact, only a small segment of the road in the western part of the AoI, some ridges and flat areas could be classified as stable areas (c.f. Fig. 1)

3.2.2 Point-cloud processing and change detection analysis

Data processing basically contained two steps, PC thinning and filtering. Point outliers and noise were manually removed. Westoby et al. (2012) demonstrated that the accuracy of a re-constructed DEM is highly correlated

with the density of points. Therefore, we aimed for a homogenous point density in all data sets. As the point densities of the 1976 (2.8 points/m^2) and 1994 (2 points/m^2) PCs differ strongly from the 2016 PC (229 points/m^2), we used a two-dimensional block filter in order to obtain uniform spatial distribution and density of points in all data sets before we filtered high and medium vegetation points. Both operations were carried out in the LIS / SAGA GIS (Laserdata.at) environment. As areas of dense vegetation generate the highest discrepancies in reconstructed DEMs (Gomez et al. 2015) we excluded forested and densely vegetated areas from all data sets. RGB values (UAS PC) were converted in HSV colour palette (Haas et al. 2011, 2016) and all points with green coded hue-values were deleted in order to eliminate points of green vegetation. To exclude non-green vegetation (dry leaves, branches, etc.) and to filter the HAP PCs we had to apply a geometrical slope-based DTM-filter that is based on a region-growing algorithm and subsequently a parameter-controlled segmentation algorithm (Neugirg et al. 2016) which classifies the PCs into ground and non-ground points. The filter compares the height of a point with the heights of all other points in a specific neighbourhood (search radius: 2.5 m) and checks wether it needs to be rejected (vegetation) or not (ground). First the height of all direct neighbours are verified before the neighbours of these neighbours are verified (Vosselmann 2000). The neighbourhood is than grown until no more points are detected within the maximum given distance (1.5 m). Co-registration of HAP PCs was done by making use of the RiSCAN PRO (Riegl, Version 2.4) integrated iterative closest point (ICP) algorithm (Multi Station Adjustment tool with plane patch filter; reference PC: 2016 stable areas). The plane patch filter approach can be separated in following steps: First, cubes of a specific start search-size (8 m) are distributed over the original PCs and a plane is best-fitted to all points within a cube. All points within a cube are than compared to the respective plane and the StD (between points and plane) is calculated. The prior defined restriction parameters maximum plane error (StD of points represented by a plane; here: 0.02 m) and minimum number of points (n=10) are used to decide wether to accept the plane or to divide the cube into 8 smaller cubes and repeat the process until the minimum search cube size (1 m) or the minimum number of points per plane value is reached. If a plane fullfills the restriction parameters a normal vector is computed at the center of gravity of the respective plane. Next, a least-squares algorithm (Zhang 1994) was used to identify the transformation parameters of the stable area surface normals (orientation and translation; scaling was not enabled) of the HAP data. If the angle between the surface normal of two planes is smaller than 5° the two planes are considered to correspond and will be used for the co-registration of PCs. Thus, only points of similar orientation are considered for the minimization of point differences in the ICP process. Finaly, all PCs were aggregated to DEMs of 1 m resolution using a bilinear resampling scheme (Conrad et al. 2015). If multiple points correspond to one grid cell the minimum elevation value of the respective points was used for the aggregation. Grid size was chosen according to the minimum point densities in order to keep the no-data areas at a minimum level and the DEM resolution as high as possible. DEMs of differences (DoDs) were calculated on basis of congruent DEMs for the entire AoI (1976 to 2016) and a single calanco, further referred to as calanco rotation (CR) for the periods 1976 to 1994, 1994 to 2016 and 1976 to 2016. The term *calanco rotation* relates to the rotational slide at the tributary head which we assume to be greatly responsible for the geomorphic development of this valley. Spatial analyses were carried out with the SAGA LIS/GIS integrated terrain analysis toolbox and include the calculation of the local morphometric terrain parameters slope and aspect. Digital mapping was conducted in ArcGIS/ArcMAP 10.3 (ESRI) and include the digitization of calanchi boundaries in order to define the calanchi extent in the respective years and to address the spatial badland development within the period 1976–2016. Several field inspections (between 2014/04 and 2016/04) allowed us to identify key geomorphic processes that are responsible for the development of the study site but also for the individual tributaries. Digital cross profiles were drawn in order to show the lateral morphometric changes within certain tributaries and enabled us to classify the single tributaries according to the classification of Rodolfi & Frascati (1979) and Moretti & Rodolfi (2000). Nevertheless, a single profile might not be representative for the geomorphic changes in the entire valley. Depending on the location of the profile it will represent the erosion, transport or deposition zone. In contrast to Ciccacci et al. (2008) and based on the available data for the entire AoI, we derived the profiles not only for one time-step but for two different time steps (1976 and 2016) in order to describe the morphological changes that have occurred in the respective valley and to classify each calanco according to the "calanchi-evolution-model" (Ciccacci et al. 2009) which describes the development from a specific type to another.

3.2.3 Uncertainty analysis and sediment balancing

As all PCs contain measurement errors which propagate into the resulting DEMs and sediment yields (Haas et al. 2016), these uncertainties need to be quantified. Uncertainty analysis was carried out according to the workflow described in Haas et al. 2016, based on the principles of Lane et al. (2003). We assume that the errors of the grid

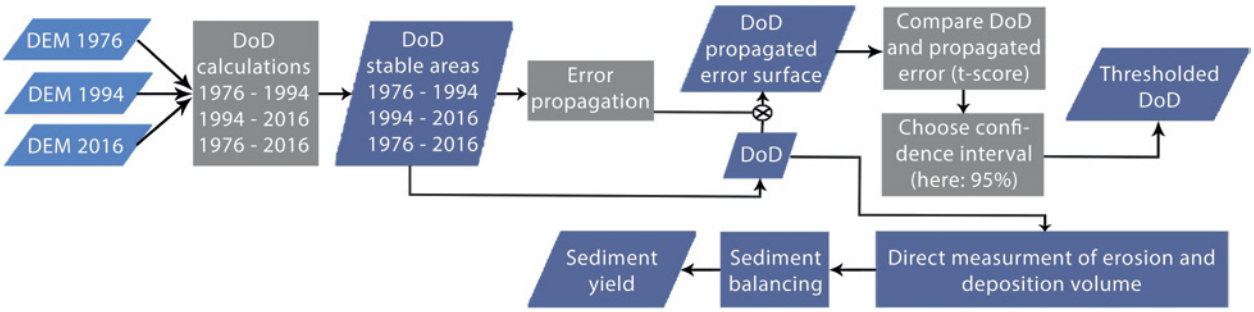

Fig. 5. Workflow data analysis – thresholded DEM of differences calculation and sediment balancing.

cells follow a normal distribution with a mean of zero and that the overall DEM error can be expressed by a standard deviation (Taylor 1997). The errors of the individual DEMs can be estimated via repeated measurements of unchanged surfaces or with stable areas (Westaway et al. 2000). As the survey design did not allow repeated observations, the stable area approach was used to address a level of detection (LoD) (Brasington et al. 2003, Lane et al. 2003, Wheaton et al. 2009, Bennett et al. 2012), also referred to as limit of detection or limit of quantification (Shrivastava & Gupta 2011). The value of each grid cell in the DoD can be converted to a t-value (Bennett et al. 2012):

$$\delta_{DoD} = \sqrt{\delta_1^2 + \delta_2^2} \quad \text{(Eq. 1)}$$

with δ_{DoD} being the mean of standard deviations of the stable areas (mean StD of all grid cells and CPs) in the respective periods ($\delta_{DoD1976–1994}$, $\delta_{DoD1994–2016}$, $\delta_{DoD1976–2016}$). A two-tailed t-test is conducted for each cell to address if a cell's change is significant (real surface change) or not (measurement error). In this study, we used a probabilistic threshold at the 95% confidence interval which corresponds to a t-critical of 1.96. Only cells with a t-value >1.96 are assumed to represent real surface changes and are used for change detection analysis (thresholded DoDs). The previously mentioned LoD can be calculated according to Lane et al. (2003)

$$t = \frac{z_1 - z_2}{\delta_{DoD}} \quad \text{(Eq. 2).}$$

Sediment balancing (Fig. 5) was carried out for the entire AoI and a single tributary on the basis of the calculated DoDs. The DoDs enable change-detection analysis for each grid cell and to calculate the related sediment yields and surface changes.

4 Results

4.1 Point-cloud processing and surface reconstruction

Image processing resulted in different PC densities and GCP accuracies (Tables 3, 4) for the respective data sets. The GCP accuracy in image space was below 1 pixel in all data sets. After point-cloud thinning the density was at 6 points per raster cell (1 m²) for the UAS data. The georeferenced orthomosaics were exported as TIFF files with the best available resolutions of 0.30 m (1976) and 0.78 m (1994). Co-registration led to a standard deviation of 0.57 m for the 1976 and 0.96 m for the 1994 stable areas resulting in LoDs between 1.12 m (1976–2016) and 2.10 m (1976–1994) (Table 4). Closer inspection of the derived DEMs revealed incorrect surface structures in certain areas of the 1994 DEM. At least two areas could be identified where the reconstruction of major topographic features (main ridges) was not successful because of overexposed images. To exclude incorrect reconstructed surface from change detection, we cropped the 1994 PC to the extent of one single tributary where surface reconstruction was successful, further referred to as "calanco rotation" (CR).

4.2 Change detection analysis

Figures 7 and 8 show the DoDs for the entire AoI (1976–2016) and for the subset CR in the observation periods 1976–1994, 1994–2016 and 1976–2016. Negative values are colourized in red to light green whereas positive cell values are represented by turquoise to blue colours. Raw and thresholded cut and fill volumes are reported in Table 4.

4.2.1 Surface changes between 1976 and 2016 for the entire AoI

In total, an area of 8,723 m² shows positive (blue), whereas an area of 9,283 m² shows negative cell values (red) which results in a sediment balance of –2,284 m³

Table 3. Results of the SfM-MVS processing.

Year	1976	1994	2016
Image count	5	3	262
Number of GCPs	11	11	44
GCP errors x / y / z [m]	2.21 / 2.57 / 3.71	1.59 / 1.71 / 2.43	0.07 0.08 0.26
GCP RMSE [m]	2.90	1.95	0.16
Point-cloud density [points/m^2]	2.8	2	229

Table 4. Standard deviations, arithmetic means and resulting LoD for the individual investigation periods.

Period	Standard deviation of stable areas [m]	Arithmetic mean of stable areas [m]	Standard deviation of checkpoints [m]	Resulting LoD [m]
1976–2016	0.57	0.09	0.40	1.12
1976–1994	1.07	0.19	0.73	2.10
1994–2016	0.96	0.11	0.68	1.88

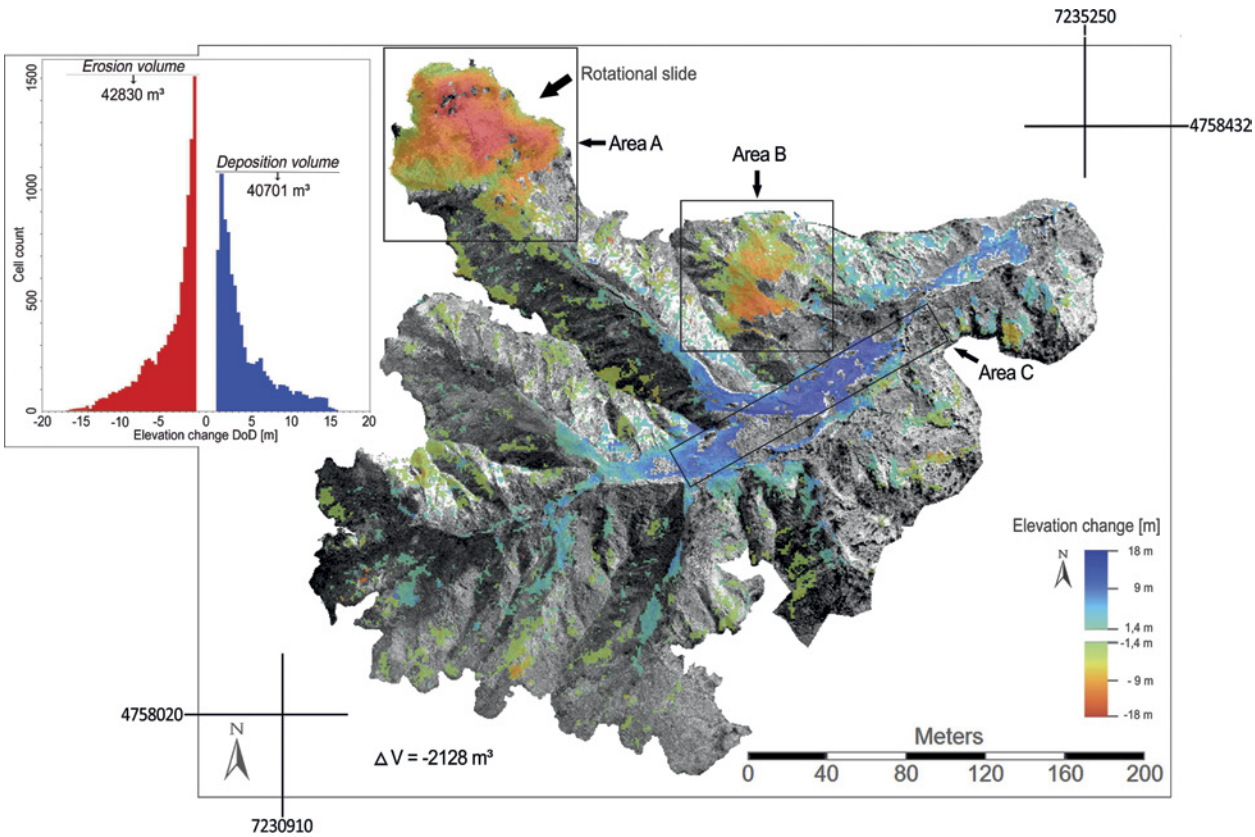

Fig. 6. Grey-scaled orthomosaic (2016) with overlaid DoD and histogram with thresholded cut and fill volumes (LoD, confidence interval 95%) for the period 1976–2016.

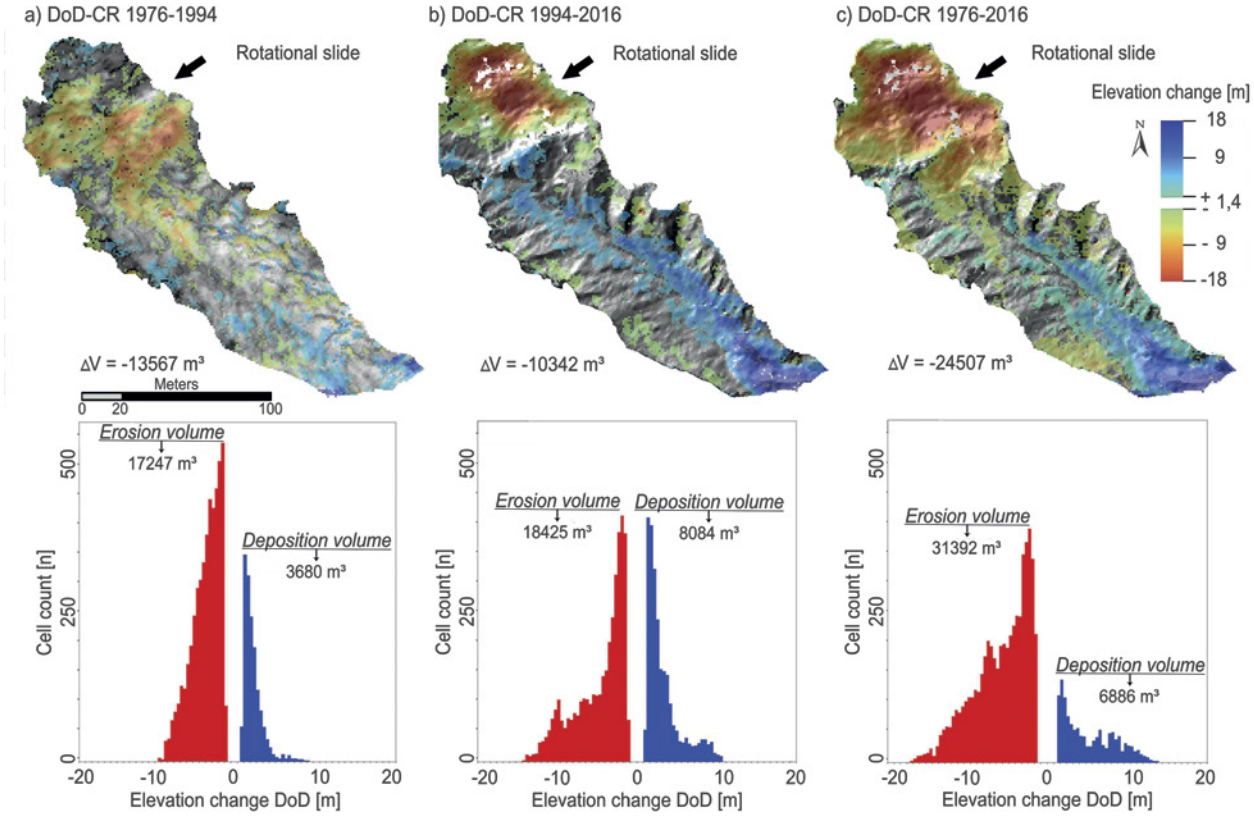

Fig. 7. Grey-scaled orthomosaic 1994 (left) and 2016 (centre and right) with overlaid DoDs and Histograms for the subset "calcanco rotation" 1976–1994 (left), 1994–2016 (centre) and 1976–2016 (right). Note that the volumes represent thresholded values (95% confidence interval).

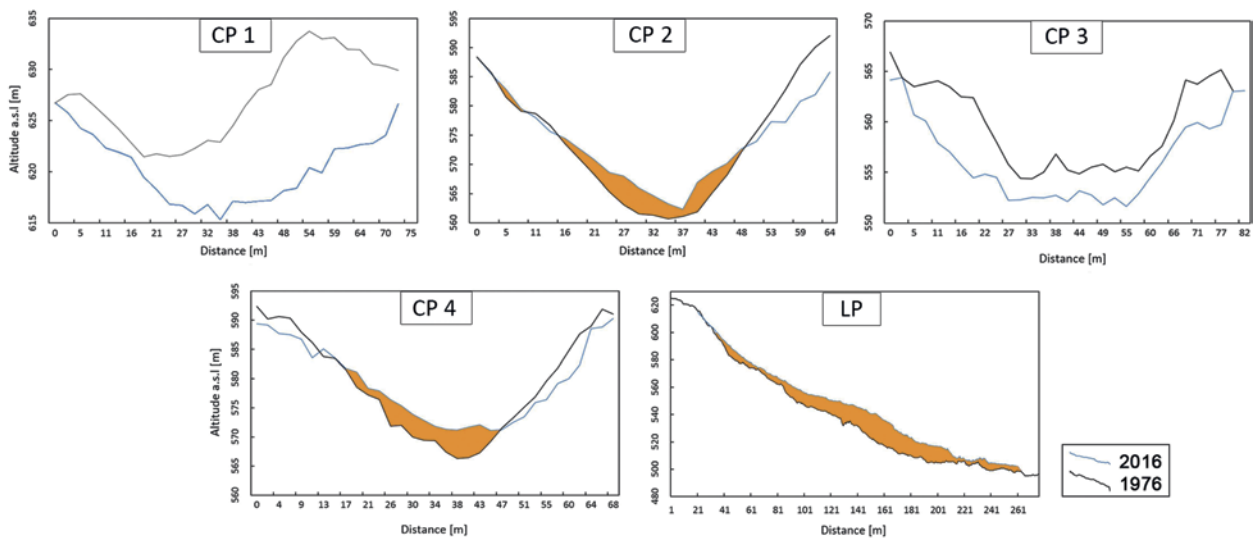

Fig. 8. Cross- and longitudinal-profiles 1976 and 2016. The orange labels mark zones of enhanced material deposition.

(Table 5) and an annual mean erosion rate of 0.01 m (Table 6). Two rotational slides could be identified through several on-site campaigns (Fig. 6, area A) where the older one is forming a flat vegetated surface, damming the younger slide which accounts for approx. 3,500 m^2. 26,749 m^3 of negative surface changes are caused by these rotational slides in the period 1976 to 2016. The upper part of the rotational slide slipped about 20 m downslope from the tear-off edge and caused a retreat of the calanco head of approx. 15 m, corresponding to a mean annual retreat rate of approx. 0.38 m for the 40 years. Excluding the rotational slides from sediment balancing results in a mean surface lowering of 0.005 $m*a^{-1}$ (Table 7).

Area B of Fig. 6 shows zones of accelerated erosion in the middle parts of the calanco slopes with maximum surface changes of –11.8 m. Erosion processes occur on the entire calanco slopes but are extensive in the slope channels. Deposition of material is most distinctive in the middle and lower parts of the main valley and reaches maximum surface changes of +16.7 m (Fig. 6, area C).

4.2.2 Surface changes between 1976 and 1994 for the subset "calanco rotation" (CR)

1976–1994

Change detection analysis for 1976 to 1994 revealed surface lowering on an area of 6,174 m^2, whereas 1,937 m^2 correspond to positive changes. The total material loss in the tributary is 18,034 m^3 (Table 5). Thereof, 15,149 m^3 account for the rotational slide. Sediment balancing lead to a mean annual erosion rate of 0.03 m (Table 6) including and 0.01 m excluding the rotational slide (Table 7). Negative changes are mainly caused by the rotational slide in the northern part of the tributary while deposition of material is concentrated on the flat surfaces on the outlet of the catchment and in the middle slope parts (Fig. 7a).

Table 5. Sediment balances of the respective time periods for the tributary CR and for the entire AoI (1976–2016).

Period	Erosion [m^3]		Accumulation [m^3]		Sediment balance [m^3]	
	Raw	Thresholded	Raw	Thresholded	Raw	Thresholded
1976–1994_CR	18,034	17,247	4,407	3,680	–13,627	–13,567
1994–2016_CR	19,162	18,425	8,744	8,084	–10,418	–10,342
1976–2016_CR	32,163	31,392	7,652	6,886	–24,510	–24,507
1976–2016_AoI	47,020	42,830	44,736	40,702	–2,284	–2,128

Table 6. Erosion volumes including the rotational slide, respective process and catchment areas and resulting mean annual surface lowering rates.

Period	With rotational slide				
	Erosion [m^3]	Net erosion area [m^2]	Study site [m^2]	Mean net surface lowering [$m*a^{-1}$]	Mean surface lowering [$m*a^{-1}$]
1976–1994_CR	18,034	6,174	14,778	0.07	0.030
1994–2016_CR	19,162	5,210	14,778	0.17	0.060
1976–2016_CR	32,163	6,582	14,778	0.12	0.050
1976–2016_AoI	47,020	15,735	109,284	0.07	0.014

Table 7. Erosion volumes excluding the rotational slide, respective process and catchment areas and resulting mean annual surface lowering rates.

Period	Without rotational slide				
	Erosion [m^3]	Net erosion area [m^2]	Study site [m^2]	Mean net surface lowering [$m*a^{-1}$]	Mean surface lowering [$m*a^{-1}$]
1976–1994_CR	2,885	2,786	14,778	0.06	0.01
1994–2016_CR	1,128	1,710	14,778	0.03	0.003
1976–2016_CR	5,414	3,032	14,778	0.05	0.009
1976–2016_AoI	20,271	12,235	109,284	0.04	0.005

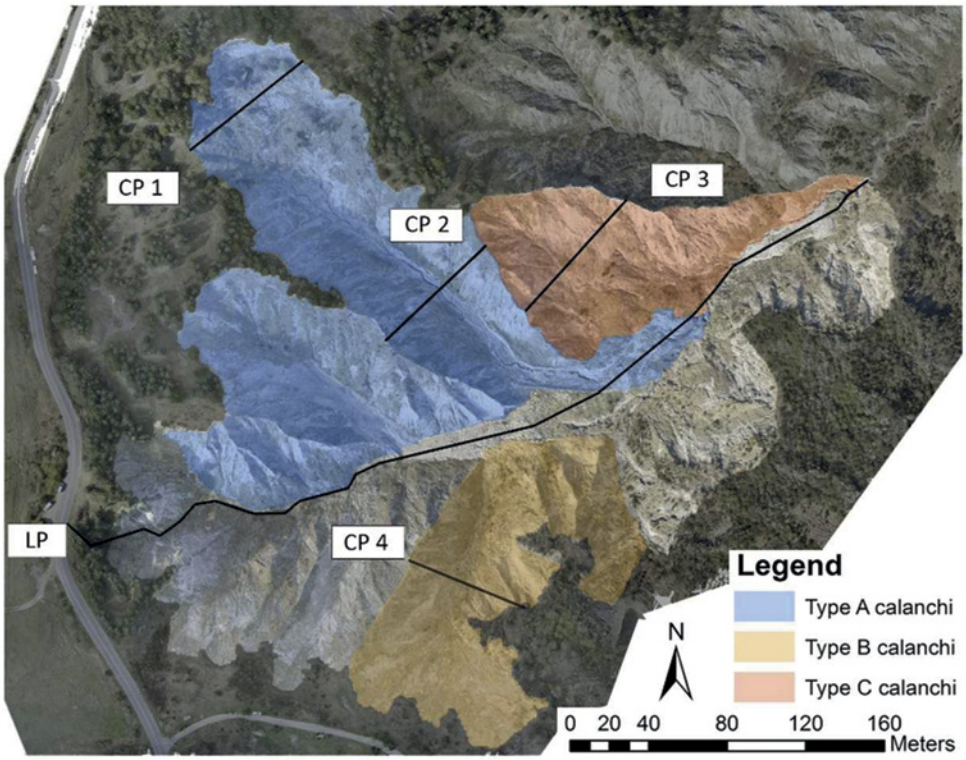

Fig. 9. Calanco landform types (according to Rodolfi & Frascati 1979; Ciccacci et al. 2008) in the AoI and location of cross-profiles.

1994–2016

The DoD computation for the period 1994 to 2016 yielded a sediment balance of –10,342 m³ (Table 5) and a mean annual erosion rate of 0.06 m (Table 6) or rather 0.003 m (Table 7) when excluding the rotational slide from the calculation. Just as in the previously analysed epoch, a majority of material loss relates to the rotational slide. Erosion, without exception, occurs on upper parts of the slopes while deposition is evident in the main channel and on the lower parts, especially in the area just below the rotational slide (Fig. 7b).

1976–2016

DEM differencing for 1976 to 2016 shows a sediment balance of –24,510 m³ (Table 5). Deposition is more pronounced in the 1994–2016 DoD and accounts for 7,652 m³ of deposited material. A material loss of 32,163 m³ resulted in a mean annual erosion rate of 0.05 m (Table 7) or rather 0.009 m if the rotational slide is excluded from the calculations (Table 7). Areas of enhanced erosion are located at the upper parts of the slope but also in the area just below the rotational slide at the beginning of the tributary's main channel. Maximum surface changes of –17.1 m per cell can be identified in the centre of the rotational slide (Fig. 7c).

4.3 Badland development

The results show very clearly that the surface along the profiles changed significantly between 1976 and 2016 (Fig. 8) and that the research area contains all three calanco types (types A, B and C) (Fig. 9). Three profiles (CP 2, CP 4 and LP) show positive changes, whereas two of them (CP 1 and CP 3) show negative changes. Note that CP1 does not refer to a special calanco type but to the evolution of the rotational slide. CP3 is located in the upper area of a tributary (Fig. 9) thus representing only the erosion zone and not the deposition zone in the valley bottom or at the foot of the slope. Due to slope gradients of 38° to 61° (derived from the 2016 DEM) most of the eroded material (area of CP3) is transported further downstream into the main valley or to the flat area of the tributary – visible in the DoD in Fig. 6 and in Fig. 10E (overgrown areas at the foot of calanco slope).

Type A calanchi with v-shaped valley floors and sharp-edged ridges (Fig. 8, CP 2) are located in the north-eastern part of the AoI and represent the predominate landforms of the catchment. Translational- and rotational slides leave areas of bare substrate and enabling secondary processes (e.g. rill erosion, piping, etc.) during rainfall events on those surfaces and enable material transport further downstream to deeper located depots in the

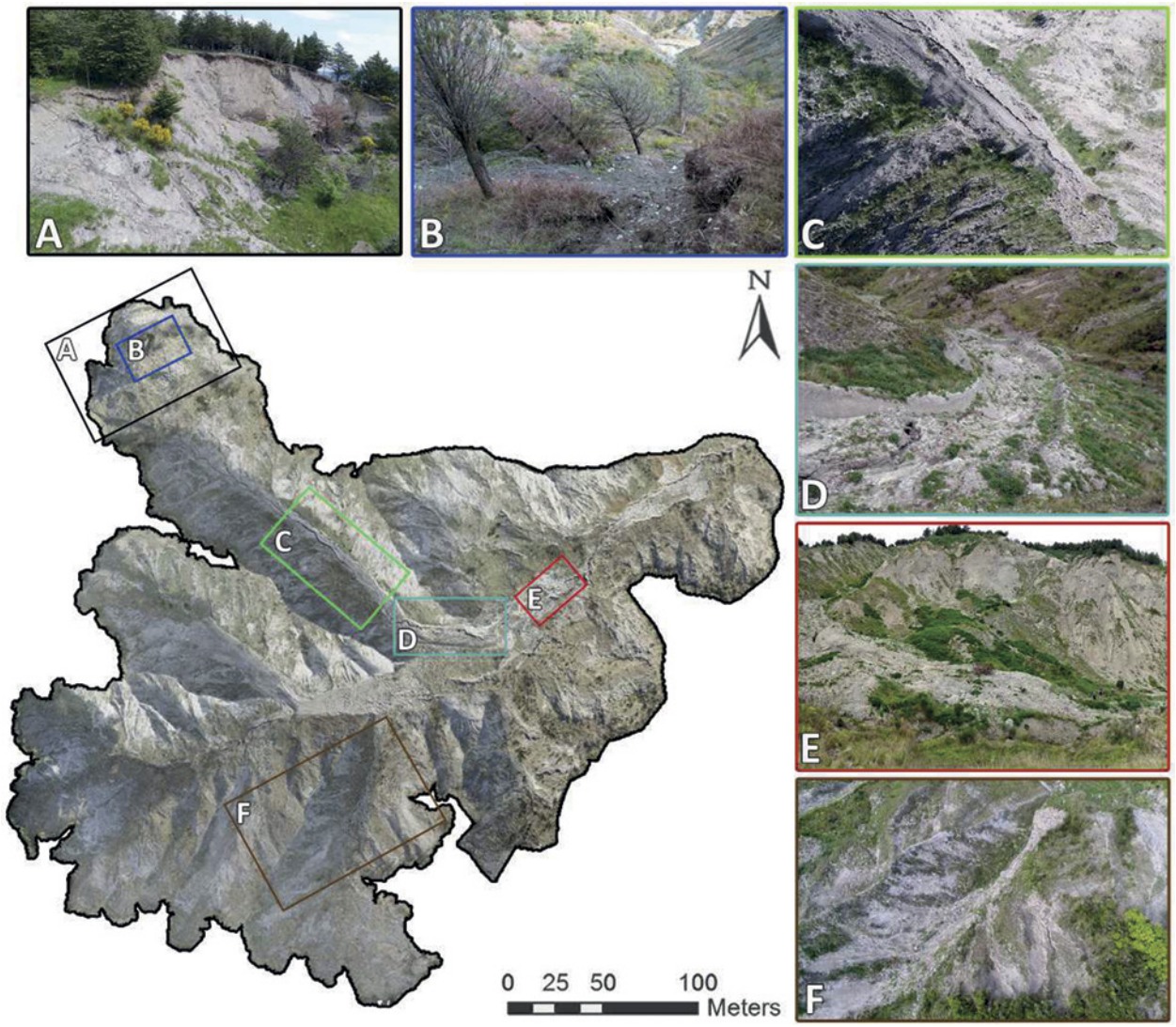

Fig. 10. Key-processes in the research area.

sediment-cascade-system (Fryirs 2013). The combination of high discharge events and sufficient availability of material within the channels lead to mud and debris type flows, which transport material downstream and produce deep valley cuttings as well as levee-like deposition areas along the transport path (Fig. 10D). Photo interpretation and several field trips between April 2014 and April 2016 confirmed the occurrence of debris flows and high activity of fluvial erosion processes (mainly rill erosion) on the bare substrate in these tributaries. However, geomorphological processes are not restricted to areas of bare soil surfaces but also occur on slopes with denser vegetation covers as in the southern part of the AoI. Here, field observations prove the occurrence of many shallow landslides on the sparsely overgrown north-facing slopes (Fig. 10F) forming a trough-shaped valley floor (Fig. 8, CP 4) which is distinctive for type B calanchi. Contrary to type A, the recurring translational slides in this zone lead to convex shaped ridges and trough valleys that are subsequently filled by deposits. Type C calanco landforms in the north-eastern part are less important landforms within the catchment. The geomorphic structures of these valleys indicate a high frequency of small landslides. Erosion is extensive on the slopes and is already in the process of destroying smaller exposed ridges within the catchment (Fig. 8, CP 3). The existence of rills on the barely vegetated slopes as well as gullies and pipes in the valley floors prove the occurrence of secondary fluvial processes both, high in frequency and magnitude within these valleys.

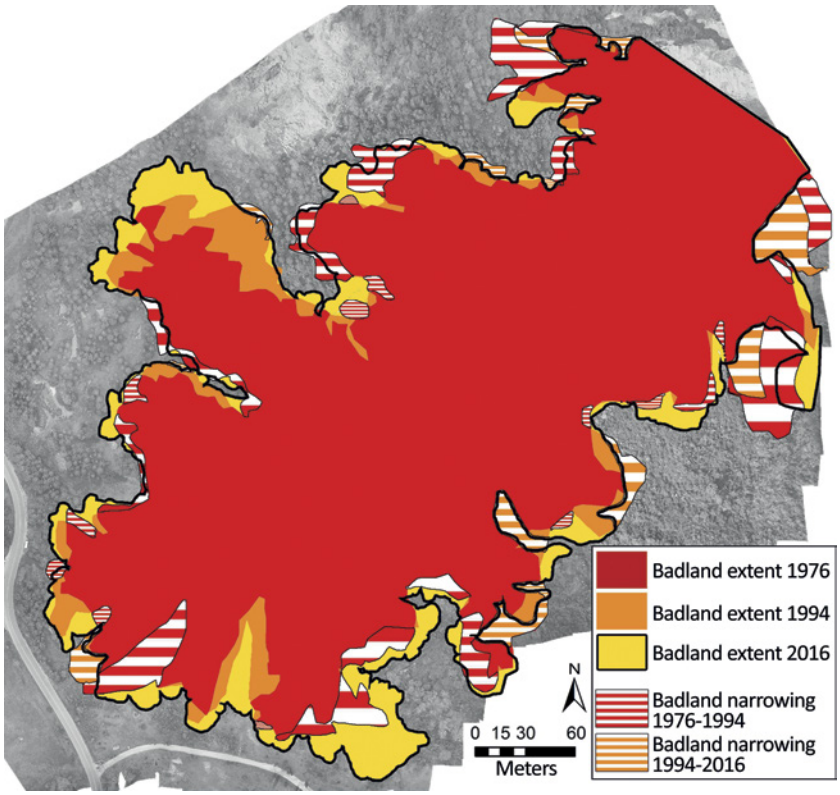

Fig. 11. Badland extent in the years 1976, 1994 and 2016.

The analysis of a longitudinal profile (LP) (Fig. 8 and 9) in the years 1976 and 2016 also confirms the "calanchi-evolution-model" as the LP clearly proves the filling of the main valley. The development of large, relatively even sediment depots in these zones resulted in a decrease of the mean slope gradient from 25° in 1976 to 14° in 2016. However, these deposits get reworked by channel incision and the development of large pipes and tunnels.

Apart from some small fragmented areas (Fig. 11, hedged polygons) near the tear-off-edge reforestation practices that have been carried out since the late '70s (Vergari et al. 2013, Aucelli et al. 2016) did not result in reduced erosion activity nor badland expansion. Anthropogenic attempts to prevent accelerated erosion processes were not successful. Even if some measures helped to reduce badland expansion and erosion activity in the first years after they were established, the practices cannot be seen as successful in terms of long-term erosion controls (Table 8).

4.4 Precipitation data

Precipitation data were acquired by the *Servizio Idrologico Regionale* at the two pluviometric stations of Spineta (1979–1999: *Spineta 1*, latitude 42°56'55" N; longitude 11°50'48" E; Altitude: 612 m a.s.l./ 2002–2016: *Spineta 2*, latitude: 42°57'04" N; longitude: 11°51'10" E; Altitude: 633 m a.s.l.), 9 km west of the study site and are provided as daily sums (www.sir.toscana.it). We calculated the climate normal (1961–1990) for a better understanding of local precipitation variations and to relate the current conditions to long term climate developments. Rainfall amounts were added up to monthly and yearly sums in order to calculate the respective averages (Fig. 12, Table 9). A simple time series analysis regarding the detection of extreme values (daily to annual scale) was conducted to identify geomorphic relevant phases. Mean daily rainfall amounts were calculated for each month and all daily extreme events were filtered on the basis of the 95% percentile threshold (Table 10). Unfortunately, there was no data available for the periods 1976 to 1978 and January 1999 to April 2002.

5 Discussion

5.1 Data processing and accuracy assessment

Concerning the uncalibrated, non-georeferenced aerial images, Photoscan Pro (now Metashape) has proven to be an effective tool for the reconstruction of the past badland topography. Scaling and global positioning via GCPs was successful for all image sets with a final global

Table 8. Shape areas (AoIs) and growth rates (1976–2015).

Year:	Extent [m²]	Change extent [m²]	Mean growth rate [m²/year]
1976	102.973	–	–
1994	102.165	–808	–44.89
2016	108.449	6.284	285.64
Overall change (1976–2016):		5.476	136.90

Table 9. Precipitation data at the station Spineta 1 (1951–1999) and 2 (2002–2016) for the observation periods.

Period:	Annual mean [mm]	Annual max. [mm]	Annual min. [mm]	Days exceeding >48 mm precipitation	Annual mean (count) of days with >48 mm precipitation
1976–1994	819.9	1883.6	589	25	1.67
1994–2016	895.5	1481.8	577.6	28	1.27
1979–2016	831.2	1883.6	577.6	53	1.41

Table 10. Monthly precipitation above the 95% percentile threshold.

Year	2004	2005	2008	2010	2014
Month	11	11 | 12	11 | 12	01 | 11	02 | 11
Precipitation [mm]	269.4	268.4 | 197.6	220.8 | 242.8	225.8 | 290.0	192.8 | 218.2

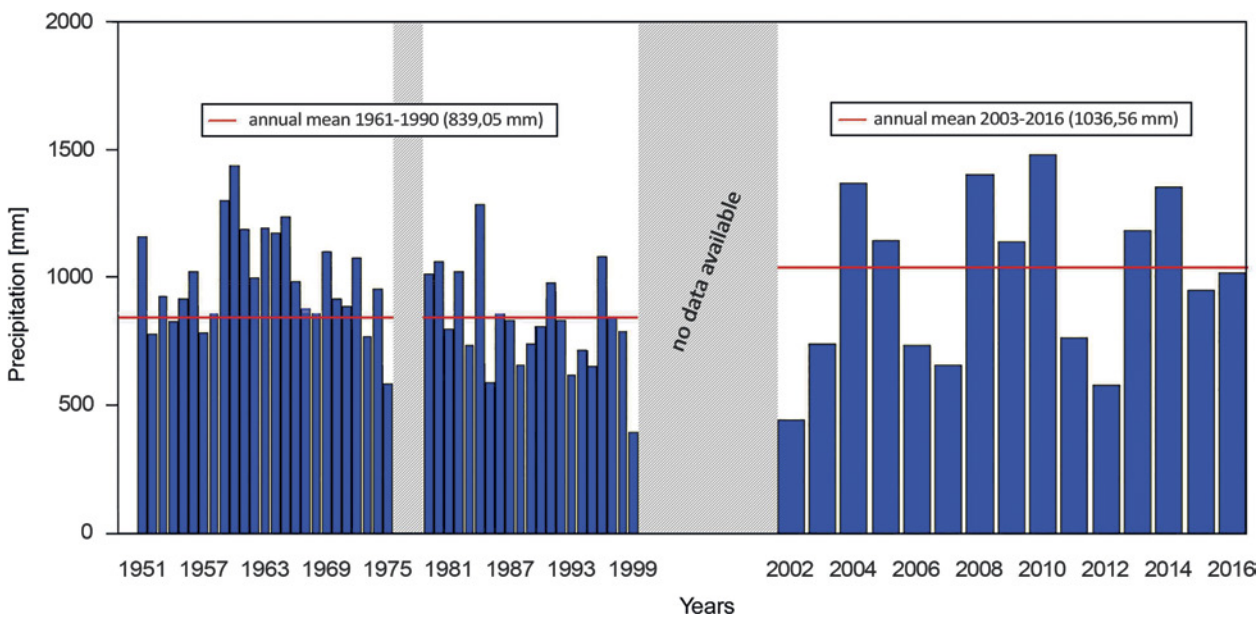

Fig. 12. Annual cumulative precipitation 1951–2016 (1951–1999: Station 1/ 42°56'55" N, 11°50'48" E, 612 m a.s.l; 2002–2016: Station 2/ 42°57'04" N, 11°51'10" E, 633 m a.s.l.).

registration RMSEs of below 1 m for all data sets. Nevertheless, the image-based surface reconstruction carried out on the two sets of HAP provided mixed outcomes which will be discussed in detail henceforth. Thorough investigations on the 1994 DEM proved our previous assumption that certain surfaces reconstruction failed in two slope parts (Fig. 13A). Closer consideration of these areas revealed that the error-prone reconstructions can be directly associated with low image quality, more specifically image resolution and texture (exposure and contrast). As those two parameters (resolution and texture) are directly linked to flying altitude, more specifically image scale we assume, that wrongly reconstructed surfaces in the 1994 data set are due to a relatively high

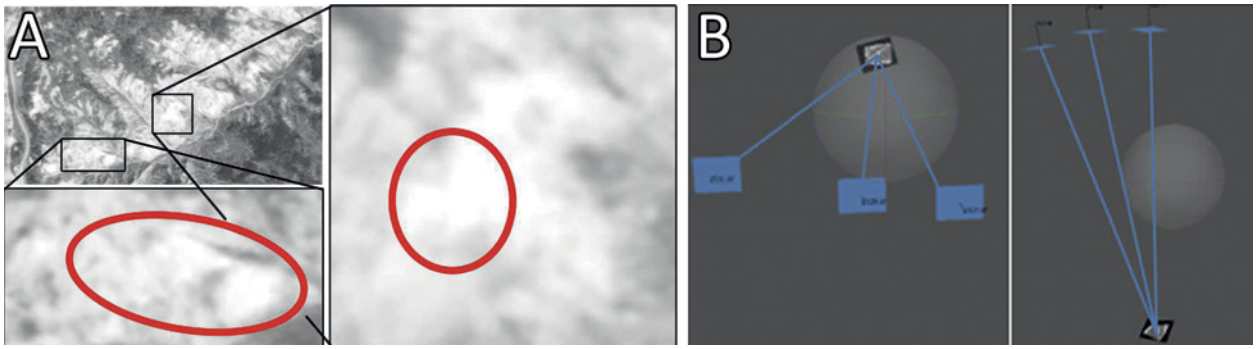

Fig. 13. Aerial image 1994 showing areas suffering from overexposure and low contrast (A: red circles) and camera positions and lines of sight for the 1994 aerial images (B: birds-eye / C: horizontal).

flight altitude (1976: 3,119 m / 1994: 5,769 m). The same effect was observed by Smith & Vericat (2015) who analysed the role of survey range on survey quality and witnessed a clear decrease of data precision with increasing survey heights.

Low image quality and resolution is a challenging factor for the edge-detection algorithms used to identify objects in photographs and subsequently the positioning of these objects in 3D (Gomez et al. 2015). This is in concordance with Bakker & Lane (2017) and Westoby et al. (2012) who both point out the importance of image texture for the bundle adjustment and feature extractions in the SfM process.

A low image count (Haas et al. 2016) of the 1994 data set, the lack of a central projection of the AoI (Fig. 13B) in the aerial images together with a relatively low image overlap of approx. 60% further contributes to the poor 3D reconstruction results as high image overlaps enable the redundancy of tie-points which again prevents errors in feature matching (Mölg & Bolch 2017). In sum, the previously mentioned drawbacks concerning an accurate surface reconstruction can be associated with the configuration design of classical photogrammetric data acquisition (low image overlap and texture) and the uneven distribution of stable areas. In order to identify surface changes between 1976 and 1994 as well as between 1994 and 2016, we defined a subset (single calanco) where surface reconstruction was successful in all areas.

5.2 Change detection and surface lowerings

5.2.1 Surface changes in the AoI between 1976 and 2016

The 1976 data enabled a successful reconstruction of topography and change detection analysis for the entire AoI in the period 1976 to 2016. The calculated mean annual precipitation amount for the respective period is 831.2 mm and rainfall exceeded 48 mm on a mean of 1.41 days*a^{-1} with a total count of 53 days. Two rotational slides (Fig. 6, area A) caused extensive surface changes on a area of approx. 4,500 m^2, corresponding to a share of 4.1% on the entire AoI. An exclusion of this area lead to an average surface lowering rate of 0.04 m*a^{-1}, which is in good concordance with the values obtained by other authors in comparable studies, for example, Aucelli et al. (2016): 0.062 m*a^{-1}, Ciccacci et al. (2008): 0.053 m*a^{-1} or Llena et al. (2020): 0.042 m*a^{-1} but exceeds these rates by including the surface changes by the major slide (0.07 m*a^{-1}). Neugirg et al. (2016) stated that the combination of impermeable layers in the sedimentary rocks and heavy rainfall or snow melting favour the occurrence of rotational slides in the clayey substrata of the Val d'Orcia badlands adjacent to the groundwater layers. On-site investigations confirmed the presence of several layers of clayey-sedimentary rock passing almost parallel to the respective slope contours. A lithologically similar layer crops out in the middle part of area B in Fig. 6 adjacent to two major erosion complexes. The varying erosion resistance of the sediment (layers) in this area leads to the conclusion that, here, erosion processes highly depend on lithological conditions and the abundance of a comprehensive vegetation cover. From this point of view, the pattern of erosion is comprehensible as surface changes are likely to be caused by the collapse of certain lithological layers and small landslides. Fine-grained substrata erode at the channel heads just below the sedimentary rock layers and get deposited in the flat channel outlets once the transport medium loses the required transport capacity (Fig. 6, north-eastern of area C). Above the sedimentary rock layer, the DoD does not show a pattern of erosion. Areas experiencing erosion are located along the ridges

Fig. 14. Piping, and mud cracks in the unsorted, coarse material within the deposition zones of the main valley (left) and tributaries (right).

and at the top of the mainly south-east facing slopes but also on top of the north-facing slopes in the south of the AoI. Here, vegetation seems to be a stabilizing factor against fluvial erosion processes and most of the surface changes in these areas are caused by translational landslides, debris and mudflows, as well as by the already mentioned mixed processes. Large patches of deposited material in the channels of the respective tributaries prove the occurrence of debris and shallow landslides. Due to the northern aspect and relatively low income of solar radiation these slopes are characterized by higher soil moisture than south-facing slopes. This again results in dense vegetation cover and comparatively high infiltration rates as surface runoff can easily infiltrate along the rootsof the plants. Those infiltration paths lead to favourable conditions for the occurrence of shallow mass movements on the lower root border (Della Seta et al. 2009, Vergari et al. 2013) followed by secondary fluvial erosion processes on the exposed substrate. The erosional pattern of Fig. 6 indicates that geomorphic processes and the related spatio-temporal development of the study site are controlled by a function of vegetation (Gallart et al. 2013), discharge, lithological conditions (De Santis et al. 2010) and slope-channel gradients (Fox & Bryan 2000).

The existence of a 12 m wide floor delimited by levees with a vertical extension of approx. 2 m (Fig. 6, area C) supports the assumption of frequently occurring debris flows and mudflows that filled the valley floor with sediments up to +16.7 m (Fig. 8, LP). Most of the mobilized material does not leave the AoI and is stored in the main valley where the deposits are already reworked by secondary high-frequency events such as fluvial erosion processes, mainly gullying and piping (Fig. 14). The existence of large pipes and gullies could be verified during several on-site investigations. The reshaping of this area is controlled by a variety of processes in the northwestern located tributaries which, of course, overlap in time and space. However, the low temporal resolution within the 40 years does not allow for a distinction of individual geomorphic processes.

Due to DoD thresholding, some areas which are affected by fluvial erosion processes might not be visualized in Figures 6 and 7 which can be attributed to two phenomena, (i) bulk density and (ii) process dynamics. Neugirg et al. (2016) showed that bulk densities range from 1.86 g*cm^{-3} (pending rock) to 1.39 g*cm^{-3} (deposition zones). The second phenomenon is related to fluvial overland processes following dry conditions which can only (re)move small particles of the clay-fraction. As a consequence, the resulting DoD values are, especially on gentle slopes, below the LoD. Contrarily, in most deposition zones the DoD values are greater than the LoD, as deposition processes frequently occur concentrated in the channels and at the already existing debris cones or at the main valley floor. Consequently, the LoD of 1.12 m enables the identification of significant surface changes either caused by high-magnitude events (surface changes above the LoD) or the frequent occurrence of lwo-magnitude events (e.g. rill- and sheet-erosion) that exceed the LoD when a specific minimum observation period (Ope_{min}) is taken into account

$$Ope_{min} = LoD*(Er_{a-mean})^{-1} \text{ (Eq. 3)}$$

with $Er_{a–mean}$ = annual mean erosion rate/surface lowering. According to equation 3, the minimum observation period for the calculation of surface changes on the basis of HAP in combination with UAS images arrives at 28 years for the catchment scale and 24 years for the slope scale when focussing on low magnitude events only. If we aim for a more comprehensive analysis which aims to detect high-frequency events too, we would have to either consider longer time intervals or refrain from DoD thresholding. Anderson (2019) emphasizes on the importance of thresholding DoDs when estimating total erosion or deposition but that the practice of thresholding also has real potential to degrade estimates of net change and associated uncertainty, and should therefore not be used for net change analysis. He also tested how the application of a threshold affects the accuracy of sums of changes and points out that thresholding enhances the potential of introducing more than removing error when assessing net changes and that non-significant measurements cannot necessarily be interpreted as areas of "no change" as they only indicate that we cannot say if changes are real or not. If we now remove non-significant measurements from net change calculations, we treat these areas as if the changes that occurred on them were exactly zero which is very unrealistic, especially in long-term analysis of natural landscapes.

5.2.2 Tributary "calanco rotation" (CR)

Fig. 7 shows the DoDs for the tributary CR. The different patterns of surface changes may result from varying dominant processes affecting the tributary in the individual periods and will be discussed in the following sections.

1976–1994

Erosion is most distinctive at the upper slope parts with maximum surface changes of approx. –10 m (Fig. 7, a). The 1994 orthomosaic shows many small scattered areas of bare substrate on the south-west facing slopes with surface changes below the LoD. Even if the DoD does not show significant changes in these barely vegetated patches it is very probably that they are affected by fluvial processes of low magnitude. Although elevation changes on these cells are small, they contribute to the overall sediment balance and should not be overlooked (Anderson 2019). Normally, fluvial overland processes are connected to heavy rainfall events that occur after longer dryperiods when a sufficient amount of unconsolidated clay particles are available for material transport.

Our precipitation analysis confirmed the lack of persistent rainfall events within this observation period. Monthly sums above the 95% percentile could not be observed while the number of days exceeding 48 mm of rain are at a maximum level (Table 9).

This led to the assumption that gravitational slides and debris-type mudflows, as well as intermediate processesof these are rare within this period as they favour sufficient soil moisture as a result of persistent rainfall. Our findings are in concordance with the results of Bollati et al. (2016) who stated that surface runoff and fluvial erosion processes were predominant in the time span of 1985–1998, while larger mass movements began to shape the area in the mid-'90s. Highest elevation changes are located in the slopes middle parts where cells show negative changes in the range of –1.12 m to –8.13 m. It is quite interesting that most upper parts of the northeast facing slopes and some areas in the north, just below the calanco tear-off-edge, show positive DoD values up to +1.47 m. This points towards three possible phenomena:

(i) Error-prone surface reconstruction of these areas due to low quality of the 1994 input data and/or (ii) registration uncertainties due to the lack of evenly distributed stable areas or (iii) vegetation that was not recognised by the filter algorithms. The calculated mean surface lowering rate of 0.03 $m*a^{-1}$ are lower than the rates obtained by Ciccacci et al. (2008) (5.5 cm a^{-1}) and Aucelli et al. (2016) (6.2 cm a^{-1}).

1994–2016

The erosional pattern and values of the 1976–1994 DoD (Fig. 7b) indicate an increase of process intensity and dynamics with a clear shift of major erosional zones to the tributary'suppermost parts after 1994. The continuous slope instability of the most northern part led to a sequence of rotational slides and to the dying of all trees in theaffected area until May 2015 (Fig. 13A, B). Many small scattered areas of negative cell values in the range of –1.14 to –3.01 m can be identified at the slope's middle positions. Positive cell values of 1.12 to 5.48 m at the slope channel outlets point to much higher process activity when compared to the time period 1976–1994. Maximum positive DoD values of 11.1 m in the tributary outlet corroborate the occurence of high-magnitude processes (debris-like levee, slope collapses, intense piping and rotational slides) in this period which could be confirmed on several on-site investigations (Fig. 14). Precipitation analysis points towards a strong influence of changed rainfall conditions on process dynamics as the mean annual rainfall (895.5 mm) increases by 9.22% when compared to the period of 1979–1994 (819.9 mm) and by 7.74% when compared to the overall observation period of 1979–2016 (831.2 mm). Considering monthly precipitation, numerous (winter) months with values above the 95% percentile threshold (193 mm) become evident (Table 10). Reasons for the high values are: (i) periods of consecutive days with precipitation sums above the average from September to November 2010 (sum: 485 mm; monthly mean: 161.67 mm) and (ii) events

with daily rainfall amounts above the average. It is quite noticeable that daily rainfall exceeds the value of 48 mm on 3 days in 2010, 4 days in 2014 and 3 days in 2015 while the mean for the period 1994 to 2016 is at 1.27 d*a^{-1} (Table 9). As intense rainfall events are considered to be highly responsible for the enhanced geomorphic activity we assume a high degree of geomorphological development of the study site in 2010 and the years following 2013. Our results revealed a lower mean surface lowering (0.03 m*a^{-1}) when compared to the changes in the period 1976–1994 (0.06 m*a^{-1}).

Interestingly, the relation between the surface lowering rates of the periods 1976 to 1994 and 1994 to 2016 changes when including the surface changes caused by the rotational slide. Under these preconditions, the annual mean of 1994–2016 (0.17 m*a^{-1}) almost triples the mean rate of the period 1976–1994 (0.06), which again confirms the previously made statement, that process-activity and major geomorphic modifications due to high-magnitude events were at a maximum in this period.

1976–2016

Excluding the rotational slide from the calculations results in an annual mean surface lowering of 0.05 m, which is in good agreement with the results obtained by other authors in comparable landscapes.

Max. DoD values of approx. –17 m prove the further development of the rotational slide in the uppermost part just below the recent badland tear-off edge (Fig. 7c). A comparison of geo-referenced aerial and satellite images revealed that first surface deformations occurred between 1976 and 1994 but that major mass movements started after 2001 (Fig. 15) which is in accordance with the results of our DoD analysis and with Bollati et al. (2016), whose study revealed an enhanced landslide activity with intense surface modification in the years 1997, 2000, 2005 and 2011. The distinctive pattern and shape of deposition areas (e.g. cones) indicate that surface changes are mainly caused by the occurrence of mass-wasting processes like debris and mudflows. Large levees in the outlet of the tributary prove the occurrence of debris flows or mudflows that are responsible for the filling of the main valley (Fig. 10D, E). Taking a look to the southern exposed channel systems we recognize highest erosion values at the upper parts near the channel heads. Deposition takes place where slope gradients decrease and must be separated according to the related processes. This was already done by Neugirg et al. (2016) whose analysis revealed major deposition zones at slope inclinations of 0° to 25° (debris flows), 10° to 35° (translational slides) and 25° to 45° (fluvial processes). The north-east exposed slopes, in contrast, show a different pattern of process dynamics. Distinctive slope channels are not existent. On-site investigations proved the frequent occurrence of translational slides on the north-east facing slopes. Here, the existence of shrubs and a high amount of coarse substrate lead to higher infiltration rates and consequently reduced surface runoff. Nevertheless, an increase of erosion activity cannot be explained by referring to changes in rainfall amounts only, as also underlined by Salvini (2008). In fact, Brunetti et al. (2006) recorded a slight decrease of total annual rainfall during the last decades for central Italy, while Vento et al. (2004) have highlighted an increase of the frequency and intensity of extreme rainfall events, similar to the results of this study, as well as in the number of consecutive dry days. As mentioned by Aucelli et al. (2016) these latter trends are concordantly identified as triggers and driving factors for fluvial erosion and mass-wasting processes in Mediterranean badland areas (Piccarreta et al. 2006, Della Seta et al. 2007, Bollati et al. 2012, Vergari et al. 2013). Furthermore, the complex interplay of land-use changes (re-forestation, the building of dams to diminish erosion, etc.) and variation in climate needs to be studied further, as it is very likely that erosion control installations led to a reduced geomorphic activity until their destruction in the early ’90s.

5.3 Badland development

From the low-resolution HAP, DEMs and DoDs could be derived with a raster size of 1 m. Although the spatial and temporal resolution does not allow for a distinction of geomorphic processes or their contribution to the geomorphic process-response system (Chorley & Kennedy 1971) typical land surface parameters allowed for a differentiation of calanco types.

In type A calanchi flow and slide material is either transported into the valley floor subsystem or re-deposited within the existing rills or slope channels, which in turn acts as temporal sediment-storage, -source and/or -sink (Larsen et al. 2015). A lack of sufficient precipitation will lead to the stabilization of these slopes as the deposited material cannot be removed, whereas in case of heavy rainfall, re-working of material occurs. The observed process- and landforms such as recurring translational slides, the development of convex shaped ridges and subsequently filled trough formed valleys in type B calanchi are in accordance with the “calanchi evolution model” (Ciccacci et al. 2009) in which the increased mass movements destroy calanco ridges and fill up the valley bottoms with flow deposits. Several on-site campaigns revealed the occurrence of characteristic mud-cracks of more than 30 cm depth on these deposits after a dry period of 5 days on these deposits. These cracks serve as ideal flow paths for superficial running water, enabling a high infiltration and therefore, creating favourable conditions for piping processes. Torri & Bryan (1997) noted a very close interaction between rill development and

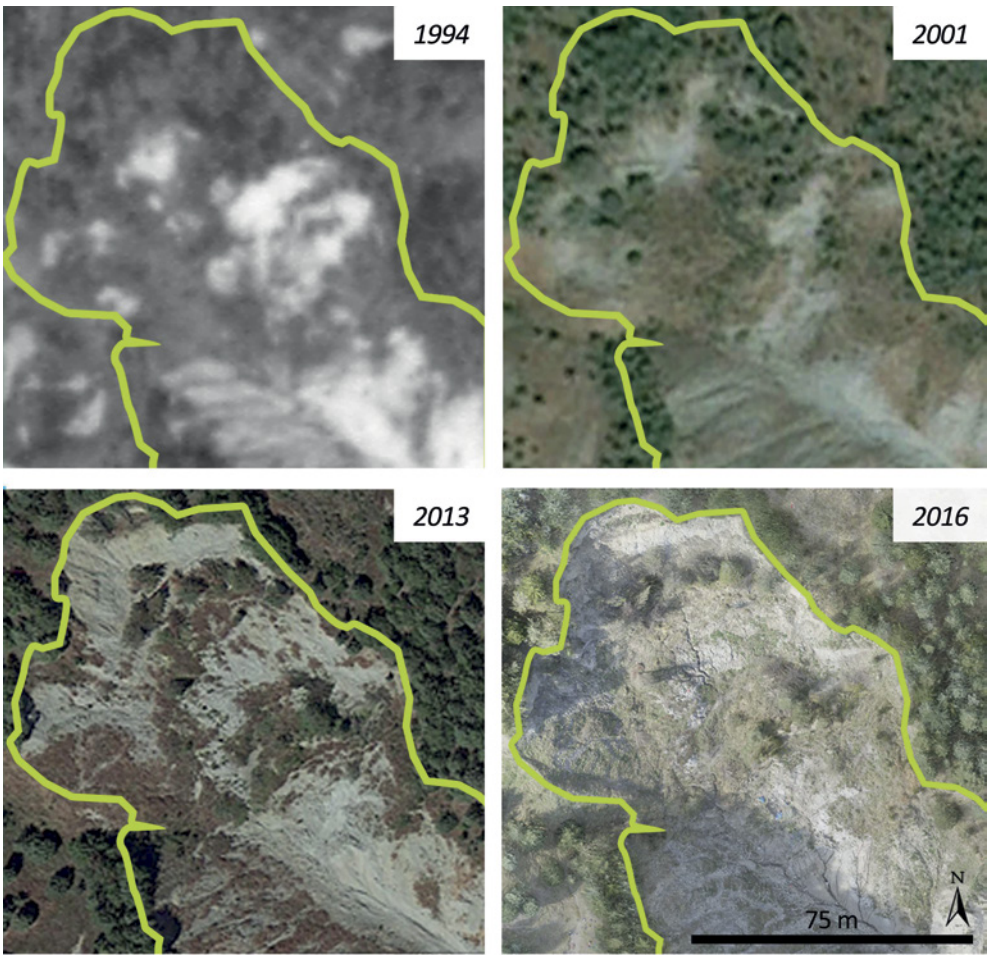

Fig. 15. Rotational slide in the years 1994 (IGM), 2001 (GoogleEarth), 2013 (GoogleEarth) and 2016 (UAV image). The yellow line marks the badland border of 2016.

micro piping on clayey biancane in Tuscany. Experimental studies at the *University of Toronto Soil Erosion Laboratory* which linked rill network development to soil water conditions (Bryan et al. 1998) have shown that both, surface and subsurface processes simultaneously influenced rill initiation, and neither the processes nor their morphological effects could be clearly separated (Bryan 2000).

In the type C calanchi the existence of rills on the barely vegetated slopes as well as gullies and pipes in the valley floors prove the occurrence of secondary fluvial processes both, high in frequency and magnitude within these valleys. The absence of distinctive filling of valley floors can be explained by the tributaries' position in the respective slope/valley-process-response system in which secondary processes rework deposited material in slope and channel positions, especially in type C calanchi (Neugirg et al. 2016). According to Fig. 11, type C calanchi can be categorized as temporary sediment stores that contribute material from the sparsely-vegetated slopes (slope-subsystem) to the main valley (valley-floor-subsystem).

Erosion control

Ciancio et al. (1984) points out, that protective reforestation can be considered successful only if the reforested areas have the ability to reproduce and to maintain a dynamic evolution of sites. Firm characteristics of the clayey soils in the study site facilitate a regressive succession of vegetation and high process dynamics in certain tributaries aggravates the re-colonization and stabilization of slopes by a dense vegetation cover. Because of the limited presence of suitable areas for tree plantations, the reforestation was carried out on small zones with a suitable substrate, only. This, of course, benefited the fragmentation and has not allowed the formation of large vegetated areas in order to contain erosion dynamics.

6 Conclusion

Methodological perspective

In this study, we conducted a long-term multi-temporal photogrammetric study to address the spatio-temporal development of a 109,000 m^2 large, semi-arid badland in central Italy. The multi-temporal quantitative analysis aimed to detect morphological changes, their spatial and temporal distribution and the assessment of long-term surface lowering rates in a semi-arid badland area in the periods of 1976–1994, 1994–2016 and 1976–2016. Therefore, two sets of grey-scaled HAP of varying spatial scale and one set of UAV images which were processed with a standart SfM-MVS software (Photoscan Pro 1.4). The analyses show that DEMs of 1 m grid size can be achieved on basis of a small set of HAP if certain quality parameters such as image-count, -overlap, GCP appearance in single images and entropy/quality of images are given. The results also show that SfM-MVS methods operate less reliable when applied to only a few images of a singular flightline with missing sidelap, low frontlap and a lack of central projection of the object or area of interest in the images.

Geomorphological perspective

Change detection analysis revealed mean surface lowering of 0.014 $m*a^{-1}$ at the catchment scale and 0.03 $m*a^{-1}$ to 0.06 $m*a^{-1}$ at slope scale, which is in good agreement with former studies in this area (c.f. Table 1). The low temporal scale of the given HAP did not allow to identify the single geomorphic processes or the exact date when they occurred, but the calculated DoDs show different patterns of erosion and deposition processes, which can be assigned to predominant geomorphic process dynamics. The LoD of 1.4 m enabled the detection of surface changes either caused by high-magnitude events with related surface changes above the LoD or the frequent occurrence of high-frequency events that exceed the LoD when a specific minimum observation period (here: 24 years on slope scale to 28 years on catchment scale) is taken into account.

The high-resolution images (UAS) allowed to identify process-related surface forms such as rills, debris cones, earth slumps/rotational slides and shallow translational slides. Landslides, both rotational and translational, are the driving forces for the spatial growth of the badland area. Erosion is enhanced in the upper parts of the tributaries and mainly caused by retreating translational slides and fluvial erosion processes while deposition zones are located in the valley bottom of the tributaries and the main valley. Intense surface runoff and high connectivity between hillslopes and channels as well as between tributaries and the main channel favour the occurrence of flooding phenomena in the valley floors. The same morphological behaviour could be observed by Faulkner (2008) and García-Ruiz et al. (2008). Due to low slope gradients, the main channel can be classified as a temporary sediment sink/store. This is in good concordance with the results of the short-term-analysis (one year) of Neugirg et al. (2016). Considering the narrow outlet of the main channel we may expect that in conditions of an average rainfall event only sediments of the sand/clay/silt-fraction will be transported further downstream. On-site investigations, shortly after a heavy rainfall event (20.2 mm in less than 1 hour) on dry surface conditions in May 2017, did not show overland flow in the main channel and consequently no transport of (coarse) sediments from the main channel to the river Orcia. Contrarily, overland flow and sediment transport was distinctive in the channels of tributaries.

Future perspective

Low-frequency and high-magnitude events (mudflows, debris flows, slides) can be considered as the driving forces of Calanchi development. For a comprehensive analyises of geomorphic processes including the contribution of low-frequency events on badland evolution, further research should focus on the extension of the investigation periods and the investigated space. Including HAP of earlier times and other calanchi systems would increase the temporal and spatial sample size and enable researchers to draw detailed conclusions about long-term development of the Calanchi landscapes in different regions and climates. Further research is needed to to analyse the badland dynamics in the context of e.g. climatic changes and how anthropogenic erosion control (reforestation, artificial constructions) influences the calanchi development in other regions.

Data availability

The presented data is part of the DFG grant HA 5740/3-1 and SCHM 1373/8-1 and will be used for the continuation of the project (DFG proposal “REGIME 4D” / in preparation). It is therfore not publicly available.

Acknowledgements: The present study was financially supported by the German Research Foundation (DFG grant numbers: HA 5740/3-1 and SCHM 1373/8-1). The fieldwork was valuably supported by Corinna Stark, Noah Stark, Hannah Stark and Verena Neugirg. As the UAS data was collected during the MSc. field course “Digital geodata: Acquisition in the field and analysis”, many master students were involved in its acquisition and are gratefully acknowledged by the authors. We thank Livia Piermattei and two anonymous reviewers for the constructive comments which significantly helped to improve the manuscript. The open access publication of this article was supported by the Open Access Fund of the Catholic University of Eichstätt-Ingolstadt.

Author contribution (according to CASRAI CRediT's definitions of contributor roles):

Author	Contributor role	Contributor role #
Manuel Stark	Conceptualization, formal analysis, investigation, methodology, project administration, visualization, writing – original draft	1, 3, 5 (lead), 6 (equal), 7, 12, 13
Fabian Neugirg	Investigation, methodology, project administration	5 (lead), 6 (equal), 7
Andreas Kaiser	Investigation, writing – review & editing	5, 14 (equal)
Marta Della Seta	Investigation, resources	5, 8
Jürgen Schmidt	Funding acquisition	4 (equal)
Michael Becht	Funding acquisition	4 (equal)
Florian Haas	Conceptualization, funding acquisition, methodology, project administration, writing – review & editing	1, 4 (equal), 6 (equal), 7, 14 (equal)
Corinna and Noah Stark and Verena Neugirg (acknowledgements)	Investigation	5

Competing interests: The authors declare that they have no conflict of interest.

References

Acocella, V., & Rossetti, F. (2002). The role of extensional tectonics at different crustal levels on granite ascent and emplacement: An example from Tuscany (Italy). *Tectonophysics, 354*(1–2), 71–83. https://doi.org/10.1016/S0040-1951(02)00290-1

Adugna, A., & Bekele, E. (2015). Assessment of recent bottlenecks and estimation of effective population size in the Ethiopian wild sorghum using simple sequence repeat allele diversity and mutation models. *Plant Genetic Resources*. https://doi.org/10.1017/S1479262115000015

Alexander, D. E. (1982). Difference between "calanchi" and "biancane" badlands in Italy. In R. B. Bryan & A. Yair (Eds.), *Badland Geomorphology and Piping* (pp. 71–87). Geobooks.

Anderson, S. W. (2019). Uncertainty in quantitative analyses of topographic change: error propagation and the role of thresholding. *Earth Surface Processes and Landforms 44*(5), 1015–1033.

Aucelli, P. P., Conforti, M., Della Seta, M., Del Monte, M., D'uva, L., Rosskopf, C. M., & Vergari, F. (2016). Multitemporal digital photogrammetric analysis for quantitative assessment of soil erosion rates in the Landola catchment of the Upper Orcia Valley (Tuscany, Italy). *Land Degradation & Development, 27*(4), 1075–1092. https://doi.org/10.1002/ldr.2324

Bakker, M., & Lane, S. N. (2017). Archival photogrammetric analysis of river–floodplain systems using Structure from Motion (SfM) methods. *Earth Surface Processes and Landforms, 42*(8), 1274–1286. https://doi.org/10.1002/esp.4085

Becht, M. (1986). Die Schwebstofführung der Gewässer im Lainbachtal bei Benediktbeuern. Münchener Geographische Abhandlungen / B; 2. München: Nelles.

Bennett, G. L., Molnar, P., Eisenbeiss, H., & McArdell, B. W. (2012). Erosional power in the Swiss Alps: Characterization of slope failure in the Illgraben. *Earth Surface Processes and Landforms, 37*(15), 1627–1640. https://doi.org/10.1002/esp.3263

Bollati, I., Della Seta, M., Pelfini, M., Del Monte, M., Fredi, P., & Palmieri, E. (2012). Dendrochronological and geomorphological investigations to assess water erosion and mass wasting processes in the Apennines of Southern Tuscany (Italy). *Catena 90,* 1–17.

Bollati, I., Vergari, F., Del Monte, M., & Pelfini, M. (2016). Multitemporal dendrogeomorphological analysis of slope instability in upper Orcia Valley (Southern Tuscany, Italy). *Geografia Fisica e Dinamica Quaternaria, 39*(2), 105–120.

Brandolini, P., Pepe, G., Capolongo, D., Cappadonia, C., Cevasco, A., Conoscenti, C., … Del Monte, M. (2018). Hillslope degradation in representative Italian areas: Just soil erosion risk or opportunity for development? *Land Degradation & Development, 29*(9), 3050–3068. https://doi.org/10.1002/ldr.2999

Brasington, J., Langham, J., & Rumsby, B. (2003). Methodological sensitivity of morphometric estimates of coarse fluvial sediment transport. *Geomorphology, 53*(3–4), 299–316. https://doi.org/10.1016/S0169-555X(02)00320-3

Brunetti, M., Maugeri, M., Monti, F., & Nanni, T. (2006). Temperature and precipitation variability in Italy in the last two centuries from homogenised instrumental time series. *International Journal of Climatology: A Journal of the Royal Meteorological Society 26*(3). https://doi.org/10.1002/joc.1251

Bucciante, M. (1922). Sulla distribuzione geografica dei calanchi in Italia. *L'Universo 38*, 585–605.

Cánovas, J. B., Stoffel, M., Martín-Duque, J. F., Corona, C., Lucía, A., Bodoque, J. M., & Montgomery, D. R. (2017). Gully evolution and geomorphic adjustments of badlands to reforestation. *Scientific reports 7*, 45027, 1–8.

Cantón, Y., Rodríguez-Caballero, E., Chamizo, S., Le Bouteiller, C., Solé-Benet, A., & Calvo-Cases, A. (2018). Runoff Generation in Badlands. In *Badlands Dynamics in a*

Context of Global Change: 155–190. Elsevier. https://doi.org/10.1016/B978-0-12-813054-4.00005-8

Castaldi, F., & Chiocchini, U. (2012). Effects of land use changes on badland erosion in clayey drainage basins, Radicofani, Central Italy. *Geomorphology 169*, 98–108.

Castiglioni, G. B. (1979). *Geomorfologia*. Unione Tipograf.-Ed. Torinese, pp. 436.

Clarke, M. L., & Rendell, H. M. (2000). The impact of the farming practice of remodelling hillslope topography on badland morphology and soil erosion processes. *Catena, 40*(2), 229–250. https://doi.org/10.1016/S0341-8162(99)00047-8

Colica, A. (2000). Analysis of the genesis and evolution of calanco morphology in an experimental area of Paiccia (Radicofani, Siena, Italy). *Geogr. Fis. Dinam. Quat. 23*, 21–32.

Cerdà, A., González-Pelayo, Ó., Giménez-Morera, A., Jordán, A., Pereira, P., Novara, A., … Ritsema, C. J. (2016). Use of barley straw residues to avoid high erosion and runoff rates on persimmon plantations in Eastern Spain under low frequency–high magnitude simulated rainfall events. *Soil Research, 54*(2), 154–165.

Ciccacci, S., Del Monte, M., & Marini, R. (2003). Erosion and recent morphological change in a sample area of the upper Orcia River basin (Southern Tuscany, Italy). *Geografia Fisica e Dinamica Quaternaria, 26*, 97–109.

Ciccacci, S., Galiano, M., Roma, M. A., & Salvatore, M. C. (2008). Morphological analysis and erosion rate evaluation in badlands of Radicofani area (Southern Tuscany—Italy). *Catena, 74*(2), 87–97. https://doi.org/10.1016/j.catena.2008.03.012

Ciccacci, S., Galiano, M., Roma, M.A., & Salvatore, M.C. (2009). Morphodynamics and morphological changes of the last 50 years in a badland sample area of Southern Tuscany (Italy). *Zeitschrift für Geomorphologie 53*, 273–297.

Conrad, O., Bechtel, B., Bock, M., Dietrich, H., Fischer, E., Gerlitz, L., … Böhner, J. (2015). System for Automated Geoscientific Analysis (SAGA) v. 2.1.4. *Geoscientific Model Development, 8*(7), 1991–2007. https://doi.org/10.5194/gmd-8-1991-2015

Della Seta, M., Del Monte, M., Fredi, P., & Palmieri, E. L. (2007). Direct and indirect evaluation of denudation rates in Central Italy. *Catena, 71*(1), 21–30. https://doi.org/10.1016/j.catena.2006.06.008

Della Seta, M., Del Monte, M., Fredi, P., & Palmieri, E. (2009). Space–time variability of denudation rates at the catchment and hillslope scales on the Tyrrhenian side of Central Italy. *Geomorphology, 107*(3–4), 161–177. https://doi.org/10.1016/j.geomorph.2008.12.004

De Santis, F., Giannossi, M. L., Medici, L., Summa, V., & Tateo, F. (2010). Impact of physico-chemical soil properties on erosion features in the Aliano area (Southern Italy). *Catena, 81*(2), 172–181. https://doi.org/10.1016/j.catena.2010.03.001

Eltner, A., & Schneider, D. (2015). Analysis of different methods for 3D reconstruction of natural surfaces from parallel-axes UAV images. *The Photogrammetric Record, 30*(151), 279–299. https://doi.org/10.1111/phor.12115

Eltner, A., Kaiser, A., Castillo, C., Rock, G., Neugirg, F., & Abellán, A. (2016). Image-based surface reconstruction in geomorphometry–merits, limits and developments. *Earth Surface Dynamics, 4*(2), 359–389. https://doi.org/10.5194/esurf-4-359-2016

Faulkner, H. (2008). Connectivity as a crucial determinant of badland morphology and evolution. *Geomorphology, 100*(1–2), 91–103. https://doi.org/10.1016/j.geomorph.2007.04.039

Faulkner, H. (2013). Badlands in marl lithologies: a field guide to soil dispersion, subsurface erosion and piping-origin gullies. *Catena, 106*, 42–53.

Faulkner, H., Alexander, R., & Wilson, B. R. (2003). Changes to the dispersive characteristics of soils along an evolutionary slope sequence in the Vera badlands, southeast Spain: Implications for site stabilisation. *Catena, 50*(2–4), 243–254. https://doi.org/10.1016/S0341-8162(02)00137-6

Fryirs, K. (2013). (Dis)Connectivity in catchment sediment cascades: a fresh look at the sediment delivery problem. *Earth Surface Processes and Landforms, 38*, 30–46.

Gallart, F., Marignani, M., Pérez-Gallego, N., Santi, E., & Maccherini, S. (2013). Thirty years of studies on badlands, from physical to vegetational approaches. A succinct review. *Catena, 106*, 4–11.

García-Ruiz, J. M., Regüés, D., Alvera, B., Lana-Renault, N., Serrano-Muela, P., Nadal-Romero, E., … Arnáez, J. (2008). Flood generation and sediment transport in experimental catchments affected by land use changes in the central Pyrenees. *Journal of Hydrology (Amsterdam), 356*(1–2), 245–260. https://doi.org/10.1016/j.jhydrol.2008.04.013

Gomez, C., Hayakawa, Y., & Obanawa, H. (2015). A study of Japanese landscapes using structure from motion derived DSMs and DEMs based on historical aerial photographs: New opportunities for vegetation monitoring and diachronic geomorphology. *Geomorphology, 242*, 11–20. https://doi.org/10.1016/j.geomorph.2015.02.021

Haas, F., Heckman, T., Becht, M., & Cyffka, B. (2011). Ground-based laserscanning – a new method for measuring fluvial erosion on steep slopes? *GRACE, Remote Sensing and Ground-based Methods in Multi-Scale Hydrology (Proceedings of Symposium J-H01 held during IUGG2011 in Melbourne, Australia, July 2011). IAHS Publ., 343*, 163–168.

Haas, F., Hilger, L., Neugirg, F., Umstädter, K., Breitung, C., Fischer, P., Hilger, P., Heckmann, T., Dusik, J., Kaiser, A., Schmidt, J., Della Seta, M., Rosenkranz, R., & Becht, M. (2016). Quantification and analysis of geomorphic processes on a recultivated iron ore mine on the Italian island Elba using long-time ground-based LIDAR and photogrammetric data by an UAV. *Nat. Hazards Earth Syst. Sci., 16*, 1269–1288.

James, M. R., & Robson, S. (2012). Straightforward reconstruction of 3D surfaces and topography with a camera: Accuracy and geoscience application. *Journal of Geophysical Research. Earth Surface, 117*(F3).

Kaiser, A., Neugirg, F., Rock, G., Müller, C., Haas, F., Ries, J., & Schmidt, J. (2014). Small-scale surface reconstruction and volume calculation of soil erosion in complex Moroccan gully morphology using structure from motion. Remote Sensing, 6, 7050–7080. https://doi.org/10.3390/rs6087050

Lane, S. N., Reid, S. C., Westaway, R. M., & Hicks, D. M. (2004). Remotely sensed topographic data for river channel

research: the identification, explanation and management of error. In R. E. J. Kelly, N. A. Drake, & S. L. Barr (Eds.), *Spatial Modelling of the Terrestrial Environment: 113–136*. West Sussex, UK: John Wiley & Sons, Ltd. https://doi.org/10.1002/0470094001.ch6

Larsen, A., Heckmann, T., Larsen, J. R., & Bork, H. R. (2016). Gully catchments as a sediment sink, not just a source: Results from a long term (~ 12 500 year) sediment budget. *Earth Surface Processes and Landforms, 41*(4), 486–498. https://doi.org/10.1002/esp.3839

Llena, M., Smith, M. W., Wheaton, J. M., & Vericat, D. (2020). Geomorphic process signatures reshaping sub-humid Mediterranean badlands: 2. Application to 5-year dataset. *Earth Surface Processes and Landforms, 45*(5), 1292–1310. https://doi.org/10.1002/esp.4822

Mölg, N., & Bolch, T. (2017). Structure-from-Motion Using Historical Aerial Images to Analyse Changes in Glacier Surface Elevation. *Remote Sensing, 9*(10), 1021. https://doi.org/10.3390/rs9101021

Moreno-de las Heras, M., & Gallart, F. (2018). The Origin of Badlands. In Nadal-Romero, E., Martínez-Murillo, J.F., & Kuhn, N.J. (eds.), *Badlands Dynamics in a Context of GlobalChange*,27–59;Elsevier.https://doi.org/10.1016/B978-0-12-813054-4.00002-2

Moretti, S. & Rodolfi, G. (2000). A typical calanchi landscape on the Eastern Apennine margin (Atri, Central Italy): geomorphological feature and evolution. *Catena, 40*, 217–228.

Nadal-Romero, E., & Regüés, D. (2010). Geomorphological dynamics of subhumid mountain badland areas–weathering, hydrological and suspended sediment transport processes: A case study in the Araguás catchment (Central Pyrenees) and implications for altered hydroclimatic regimes. *Progress in Physical Geography, 34*(2), 123–150. https://doi.org/10.1177/0309133309356624

Nebiker, S., Lack, N., & Deuber, M. (2014). Building change detection from historical aerial photographs using dense image matching and object-based image analysis. *Remote Sensing, 6*(9), 8310–8336. https://doi.org/10.3390/rs6098310

Neugirg, F., Stark, M., Kaiser, A., Vlacilova, M., Della Seta, M., Vergari, F., Schmid, M., Becht, M., & Haas, F. (2016). Erosion processes in calanchi in the Upper Orcia Valley, Southern Tuscany, Italy based on multitemporal high-resolution terrestrial LiDAR and UAV surveys. *Geomorphology 269*, 8–22.

Piccarreta, M., Faulkner, H., Bentivenga, M., & Capolongo, D. (2006). The influence of physico-chemical material properties on erosion processes in the badlands of Basilicata, Southern Italy. *Geomorphology, 81*(3–4), 235–251. https://doi.org/10.1016/j.geomorph.2006.04.010

Piermattei, L., Carturan, L., de Blasi, F., Tarolli, P., Dalla Fontana, G., Vettore, A., & Pfeifer, N. (2016). Suitability of ground-based SfM–MVS for monitoring glacial and periglacial processes. *Earth Surf. Dynam., 4*, 425–443. https://doi.org/10.5194/esurf-4-425-2016

Riegl (2016). Riegl laser measurement systems: RiSCAN PRO version. 2.4, Horn, Austria.

Rodolfi, G., & Frascati, F. (1979). Cartografia di base per la programmazione degli interventi in aree marginali area rappresentativa dell'alta Valdera: Memorie illustrative della carta geomorfologica. *Annali Instituto Sperimentale per lo Studio e la Difesa del Suolo, 10*, 37–80

Salvini, R. (2008). Analisi morfometriche delle Crete Senesi mediante remote sensing and GIS. *Memorie Descrittive della Carta Geologica d'Italia, 78*, 245–252.

Shrivastava, A., & Gupta, V. B. (2011). Methods for the determination of limit of detection and limit of quantitation of the analytical methods. *Chronicles of Young Scientists, 2*(1), 21. https://doi.org/10.4103/2229-5186.79345

Taylor, J. R. (1997). An introduction to error analysis: The study of uncertainties in physical measurements, Sausalito, CA, USA. Oxford: Oxford University Press.

Vento, D., Esposito, S., Epifani, C., & Giuseppe, E. (2004). Studio di eventuali variazioni delle strutture meteorologiche e dei regimi pluviometrici italiani. CLIMAGRI-Cambiamenti Climatici e agricoltura-Risultati attività II anno. UCEA, Roma giugno, 88-901472.

Vergari, F., Della Seta, M., Del Monte, M., & Barbieri, M. (2013). Badlands denudation "hot spots": The role of parent material properties on geomorphic processes in 20-years monitored sites of Southern Tuscany (Italy). *Catena, 106*, 31–41. https://doi.org/10.1016/j.catena.2012.02.007

Vergari, F., Della Seta, M., Del Monte, M., Fredi, P., & Palmieri, E. (2011). Landslide susceptibility assessment in the Upper Orcia Valley (Southern Tuscany, Italy) through conditional analysis: A contribution to the unbiased selection of causal factors. *Natural Hazards and Earth System Sciences, 11*(5), 1475–1497. https://doi.org/10.5194/nhess-11-1475-2011

Vosselmann (2000). Slope based filtering of laser altimetry data. IAPRS, Vol. XXXIII, Part B3, Amsterdam, The Netherlands: 935–942.

Westaway, R. M., Lane, S. N., & Hicks, D. M. (2000). The development of an automated correction procedure for digital photogrammetry for the study of wide, shallow, gravel-bed rivers. *Earth Surface Processes and Landforms 25*(2), 209–226.

Westoby, M. J., Brasington, J., Glasser, N. F., Hambrey, M. J., & Reynolds, J. M. (2012). 'Structure-from-Motion' photogrammetry: A low-cost, effective tool for geoscience applications. *Geomorphology, 179*, 300–314.

Zhang, C., & Kovacs, J. M. (2012). The application of small unmanned aerial systems for precision agriculture: A review. *Precision Agriculture, 13*(6), 693–712. https://doi.org/10.1007/s11119-012-9274-5

Zhang, B., He, C., Burnham, M., & Zhang, L. (2016). Evaluating the coupling effects of climate aridity and vegetation restoration on soil erosion over the Loess Plateau in China. *Science of the Total Environment, 539*, 436–449. https://doi.org/10.1016/j.scitotenv.2015.08.132

Manuscript received: January 16, 2020
Revisions requested: April 6, 2020
Revised version received: July 8, 2020
Accepted: July 8, 2020